JAEA-Data/Code
2025-009
DOI:10.11484/jaea-data-code-2025-009

JAEA-Data/Code

# Specifications for Benchmark Analyses of Transient Thermal-hydraulics in Reactor Vessel and Primary Heat Transport System during Decay Heat Removal Operation

Jun KOBAYASHI, Masaaki TANAKA, Erina HAMASE and Toshiki EZURE

Fast Reactor Research and Development Department
Oarai Nuclear Engineering Institute

August 2025

Japan Atomic Energy Agency

日本原子力研究開発機構

国立研究開発法人日本原子力研究開発機構　研究開発推進部　科学技術情報課
〒 319-1112　茨城県那珂郡東海村大字村松 4 番地 49
E-mail: ird-support@jaea.go.jp

JAEA-Data/Code 2025-009

# Specifications for Benchmark Analyses of Transient Thermal-hydraulics in Reactor Vessel and Primary Heat Transport System during Decay Heat Removal Operation

Jun KOBAYASHI, Masaaki TANAKA, Erina HAMASE and Toshiki EZURE

Fast Reactor Research and Development Department
Oarai Nuclear Engineering Institute
Japan Atomic Energy Agency
Oarai-machi, Higashiibaraki-gun, Ibaraki-ken

(Received May 12, 2025)

In a sodium-cooled fast reactor, a diversified auxiliary cooling system to remove decay heat from the core is required to enhance its safety. The decay heat removal systems (DHRSs) include a direct reactor auxiliary cooling system (DRACS) with a heat exchanger in the upper plenum (UP) of the reactor vessel (RV), a primary reactor auxiliary cooling system (PRACS) with a heat exchanger in the primary heat transport system (PHTS), an intermediate reactor auxiliary cooling system (IRACS) with a heat exchanger in the secondary heat transport system (SHTS), a heat removal system which employs a steam generator, and a reactor vessel auxiliary cooling system (RVACS) that effects cooling from outside the RV. In the operation of the DRACS with a dipped-type direct heat exchanger (D-DHX) installed in the UP of the RV (UP-RV), the thermal interaction, called core-plenum interaction (CPI), regarding the thermal-hydraulic phenomena in the UP-RV and the core is observed. The CPI includes the penetration flow of the sodium at a low temperature from the D-DHX into the core assemblies, the flow in the gap between assemblies, and the radial heat transfer through sodium in the gap. On the other hand, in the operation of the PRACS or IRACS, where the flowrate in the PHTS is maintained, the core coolability is affected by plant operating conditions. Two transient tests conducted at the PLANDTL-DHX sodium test facility in Japan Atomic Energy Agency were provided to develop an appropriate numerical analysis model for prediction of transient thermal-hydraulics in the DHRSs, the core, and the PHTS. In this document, the geometry information of the RV and the PHTS, including the heat exchangers for the DHRS, and the measured flowrate and temperature transients at each inlet of the intermediate heat exchanger (IHX) on the SHTS side and DHRS were specified as the boundary conditions for the benchmark analyses.

Keywords: Sodium-cooled Fast Reactor, Thermal-hydraulics, Core-plenum Interaction, Decay Heat Removal Systems, Numerical Analysis

JAEA-Data/Code 2025-009

# 崩壊熱除去運転時における原子炉容器及び１次熱輸送系の過渡熱流動を対象としたベンチマーク解析仕様書

日本原子力研究開発機構　大洗原子力工学研究所
高速炉研究開発部
小林　順、田中　正暁、浜瀬　枝里菜、江連　俊樹

（2025 年 5 月 12 日受理）

ナトリウム冷却高速炉の安全性強化の観点から、多様な崩壊熱除去システムの設置が重要となっている。崩壊熱除去システムとして、原子炉容器内に冷却器を設置する DRACS、1 次熱輸送系内に冷却器を設置する PRACS、2 次熱輸送系内に熱交換器を設置する IRACS、蒸気発生器を用いた除熱、そして原子炉容器の外側から冷却する RVACS が挙げられる。原子炉容器内の上部プレナム部に浸漬させた直接炉内冷却器（D-DHX）を用いた DRACS は、炉心入口流量の確保が要件とはならず、原子炉容器内で冷却過程が完結する利点があるが、炉心部では D-DHX からの低温ナトリウムが炉心部の集合体間の隙間に潜り込む流れ（IWF）が生じ、炉心ープレナム相互作用と呼ばれる複雑な熱流動現象を考慮することが必要となる。一方、炉心入口流量が確保される PRACS あるいは IRACS では、炉心部での複雑な熱流動現象を考慮する必要はないが、プラントの運転条件との関係が重要となる。そこで、崩壊熱除去システムと炉心部、さらにはプラント運転条件との相互作用を考慮したプラント挙動を適切に再現及び予測できる解析手法の構築を目的として、2 つの試験条件を対象としてベンチマーク解析を実施することとした。これらの試験は、日本原子力研究開発機構が所有するナトリウム試験装置（PLANDTL-DHX）にて、炉心部での集合体間径方向熱移行や IWF を含む炉内自然対流が重要となる DRACS 方式と、1 次熱輸送系の自然循環流量の確保による熱輸送が重要となる PRACS 方式を採用して、定常運転時からのスクラムを模擬したシステム過渡試験である。本報は、ベンチマーク解析の実施にあたり、モデル化に必要となる PLANDTL-DHX の試験体の形状情報（1 次熱輸送系のみ）と、計測結果に基づいて、中間熱交換器（IHX）と崩壊熱除去系の各 2 次熱輸送系入口における流量及び温度変化を解析時の境界条件として記載したものである。

大洗原子力工学研究所：〒311-1393　茨城県東茨城郡大洗町成田町 4002 番地

Contents

目　次

# Preface

The plant specifications, geometry, operating conditions, and the other data appearing in this document were created for benchmark analyses to be performed for the activities in- and out-side of the JAEA under a valid implementing arrangement of the benchmark collaboration, including international activities. JAEA notes that some of these differ from the actual specifications, fabrication dimensions, operating conditions, etc. Revision of this document, including the release of additional data, can be made at an appropriate time when JAEA recognizes the necessity. JAEA strictly assumes no liability or responsibility arising out of or in connection with the use of any information contained in the document and/or additional data.

# List of Tables

List of Figures

Acronyms

| | |
|---|---|
| AC: | Air Cooler |
| AC-DHRS: | Air Cooler in Decay Heat Removal System |
| CFD: | Computational Fluid Dynamics |
| CPI: | Core-Plenum Interaction |
| CRP: | Coordinated Research Project |
| D-DHX: | Dipped-type Direct Heat eXchanger |
| DHRS: | Decay Heat Removal System |
| DRACS: | Direct Reactor Auxiliary Cooling System |
| EMF: | Electro-Magnetic Flowmeter |
| EMP: | Electro-Magnetic Pump |
| EMP-DHRS: | Electro-Magnetic Pump in Decay Heat Removal System |
| EMP-PHTS: | Electro-Magnetic Pump in Primary Heat Transport System |
| EMP-SHTS: | Electro-Magnetic Pump in Secondary Heat Transport System |
| FC: | Forced Circulation |
| HTS: | Heat Transport System |
| IHX: | Intermediate Heat eXchanger |
| IRACS: | Intermediated Reactor Auxiliary Cooling System |
| IWF: | Inter-Wrapper Flow |
| IWG: | Inter-Wrapper Gap |
| JAEA: | Japan Atomic Energy Agency |
| LP: | Lower Plenum |
| NC: | Natural Circulation |
| P-DHX: | Penetrated-type DHX |
| PHTS: | Primary Heat Transport System |
| PHX: | Primary Heat eXchanger |
| PLANDTL-DHX: | PLANt Dynamics Test Loop with Direct core Heat eXchanger |
| PRACS: | Primary Reactor Auxiliary Cooling System |
| RHT: | Radial Heat Transfer |
| RV: | Reactor Vessel |
| RVACS: | Reactor Vessel Auxiliary Cooling System |
| SFR: | Sodium-cooled Fast Reactor |
| SG: | Steam Generator |
| SHTS: | Secondary Heat Transport System |
| SV: | Sodium Valve |
| TC: | Thermo-Couple |
| UCS: | Upper Core Structure |
| UP: | Upper Plenum |
| UP-IHX: | Upper Plenum in Intermediate Heat eXchanger |
| UP-RV: | Upper Plenum in Reactor Vessel |

## 1. Introduction

In a sodium-cooled fast reactor (SFR), a diversified decay heat removal system (DHRS) as an auxiliary cooling system to remove decay heat is required to enhance its safety. The DHRSs include a direct reactor auxiliary cooling system (DRACS) with a heat exchanger installed in the upper plenum (UP) of the reactor vessel (RV), a primary reactor auxiliary cooling system (PRACS) with a heat exchanger installed in the primary heat transport system (PHTS), an intermediate reactor auxiliary cooling system (IRACS) with a heat exchanger bypassed in the secondary heat transport system (SHTS), a heat removal system that employs a steam generator, and a reactor vessel auxiliary cooling system (RVACS) that cools the reactor vessel from outside.

In the Japan Atomic Energy Agency (JAEA), the DRACS with a dipped-type direct heat exchanger (D-DHX) installed in the UP of the RV (UP-RV) has been investigated as one of the most reliable auxiliary cooling systems in the advanced SFR being developed in Japan [1]. In addition, the IRACS and DRACS with a penetrated-type DHX (P-DHX) were also investigated for comparison. Figure 1 shows typical thermal-hydraulic phenomena in the RV of a pool-type SFR during D-DHX operation. It is known that natural circulation (NC) occurs in the RV during D-DHX operation and the thermal-hydraulic interaction between the core and UP-RV, which is called core-plenum interaction (CPI), can be observed. The CPI includes the penetration flow of low-temperature sodium from the D-DHX into the assemblies, the flow named Inter-Wrapper Flow (IWF) through the gap between the assembly wrapper tubes (IWG: Inter-Wrapper Gap), and the radial heat transfer (RHT) among these through sodium in the IWG. In the UP-RV, thermal stratification is a significant phenomenon considered in the CPI. The CPI affects the maximum temperature in the core and the NC conditions in the PHTS. The utilization of NC induced by D-DHX operation is a useful means of decay heat removal from the viewpoint of enhanced SFR reliability and safety. On the other hand, in cases where the PRACS or IRACS is installed, since the flowrate through the PHTS is maintained, the core coolability is significantly affected by the operating conditions and the CPI is no longer an issue in the UP-RV. In DHRS operation, the flowrate in the PHTS changes according to the operating conditions of the SHTS and DHRS. To evaluate the maximum temperature in the core, the interaction of the transient thermal-hydraulics in the PHTS and the core is very important.

In this document, the dimensions of the RV and the PHTS, including the heat exchangers for DHRS in the PLANDTL-DHX (PLANt Dynamics Test Loop with Direct core Heat eXchanger) scaled sodium test facility built in JAEA, are specified to implement benchmark analyses as well as the boundary conditions of the measured flowrate and temperature changes at the inlets of the intermediate heat exchanger (IHX) and DHRS on the secondary side. To develop an appropriate numerical analysis model for the prediction of transient thermal-hydraulics in the core, the PHTS, and the DHRS, two cases of transient tests using the DRACS and PRACS conducted at the PLANDTL-DHX are provided. For the benchmark analyses, one case involves DRACS operation (Case-DRACS) in which the cold sodium from the D-DHX flows into assemblies and IWG, and the other case is PRACS operation (Case-PRACS) in which the cold sodium from a heat exchanger installed in the UP of the IHX (UP-IHX) on the PHTS side sends the flow to the core in the PHTS. In Case-DRACS, the cold sodium flowing from the D-DHX occupies the lower region of the UP-RV and thermal stratification appears in it. The cold sodium from the D-DHX enters the core region. The IWF can remove the heat generated in an assembly through its wrapper tube. The RHT among assemblies through the sodium in the IWG can flatten the horizontal temperature distribution in the core, and the flowrates through the assemblies are redistributed according

to the temperature distribution in the core. In Case-PRACS, the flowrate of the PHTS regulating the maximum temperature in the core is affected by the operating conditions of the SHTS and DHRS. Complex thermal-hydraulic behavior such as the CPI is not significant in the RV.

In Sec. 2, the PLANDTL-DHX sodium test facility is outlined and the geometry of components, including the UP-RV, simulated core, lower plenum (LP) in the RV, IHX, D-DHX in the DRACS, and the primary heat exchanger (PHX) in the PRACS, are described. Moreover, other components in the PHTS, SHTS, and DHRS are also described. The measurement system and recording system are explained. In Sec. 3, selectable analysis models for benchmark analyses according to the objective of the participants, and a reference approach for the benchmark analyses is provided. In Sec. 4, locations where the flowrates and temperatures were measured are described for comparison with the numerical results. In Sec. 5, the boundary conditions for benchmark analyses are specified based on the measured data for the initial steady state and transient state in Case-DRACS and Case-PRACS.

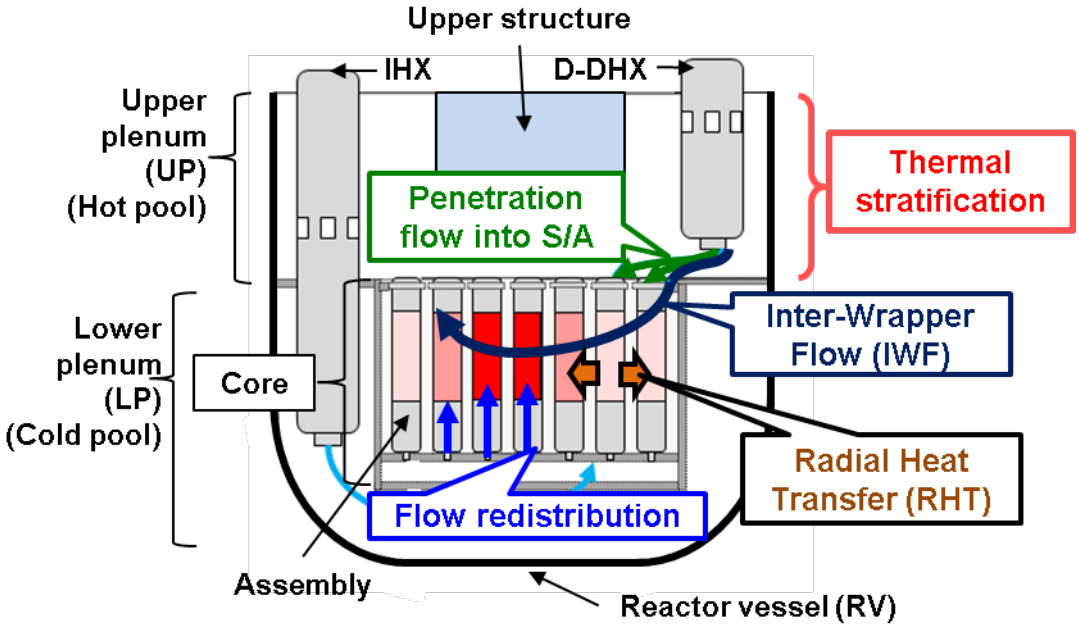


**Figure 1 Typical thermal-hydraulic phenomena called CPI in the RV during D-DHX operation.**

## 2. Description of PLANDTL-DHX

### 2.1 Outline of Test Facility

Various tests on the PLANDTL-DHX scaled sodium test facility [2, 3] had been carried out to investigate thermal-hydraulic phenomena during various plant operating conditions for decay heat removal in steady and transient states. PLANDTL-DHX was designed to simulate thermal-hydraulics in the core during transient from the forced circulation (FC) state representing a normal operation condition to the NC state for a decay heat removal operation condition. It contains major components in the heat transport systems of an SFR except for the steam generator (SG) and the water/vapor system. Significant tests using the DRACS with the D-DHX and the PRACS with the PHX had been conducted to investigate the core cooling capability in steady state and transient conditions.

Figure 2 illustrates the schematic diagram of PLANDTL-DHX. PLANDTL-DHX comprises the partial model of RV containing the simulated core equipped with seven assemblies, the UP-RV, the PHTS, the IHX, the SHTS, the DHRS with the D-DHX for the DRACS in the UP-RV, and the PHX for the PRACS in the UP-IHX on the PHTS side, the air coolers (ACs) in the SHTS and the DHRS (AC-SHTS and AC-DHRS) for heat sink, the LP of the RV, which was a vessel separately located in the PHTS, and related components: e.g., electro-magnetic pumps (EMPs), electro-magnetic flowmeters (EMFs), valves, electric sodium heaters, and sensors for liquid level, pressure, and temperature. The piping on the secondary side of the D-DHX and the PHX are connected to the AC-DHRS. Hot sodium from the assemblies flows into the UP-RV and then to the IHX through the hot-leg piping of the PHTS. In the cold-leg piping of the PHTS from the IHX outlet, low-temperature sodium enters a vessel for the LP of the RV, which is separated from the RV, and flows into the simulated core through the three lines: one to the center assembly, another to three outer assemblies of A, B, and C, and the third to the remaining three outer assemblies of D, E, and F, respectively. The heat transferred from the PHTS at the IHX is removed by the AC-SHTS. The heat from the PHTS at the D-DHX and PHX is transferred to the AC-DHRS. The devices are controlled by a digital control system and various transient changes from FC to NC are simulated by program settings.

Table 1 lists the major specifications of the PLANDTL-DHX. In the PHTS, the thermal power of the simulated core section is set to a maximum of 1.2 MW, and the primary sodium flowrate is set to a maximum of 0.02 $m^3/s$ (1200 liter/min). The heat capacity of the IHX to remove heat from the simulated core to the SHTS is 1.2 MW.

**Table 1 Major specifications of the PLANDTL-DHX sodium test facility.**

| Item | Unit | Values |
|---|---|---|
| Main structural material | - | SUS316 |
| Design maximum temperature | °C | 650 |
| Design maximum pressure | MPa | 0.8 |
| Primary loop maximum flowrate | $m^3/s$ | 0.02 |
| Secondary loop maximum flowrate | $m^3/s$ | 0.0117 |
| Core heater maximum power | MW | 1.2 |
| Number of assemblies | - | 7 |
| Heater pin heating length | m | 1.0 |
| Number of heater pins in center assembly | - | 37 |
| Number of heater pins in outer assembly | - | 7 |
| Heater pin diameter of center assembly | m | 0.0083 |
| Heater pin diameter of outer assembly | m | 0.0208 |
| Sodium inventory in dump tank | kg | 25,000 |

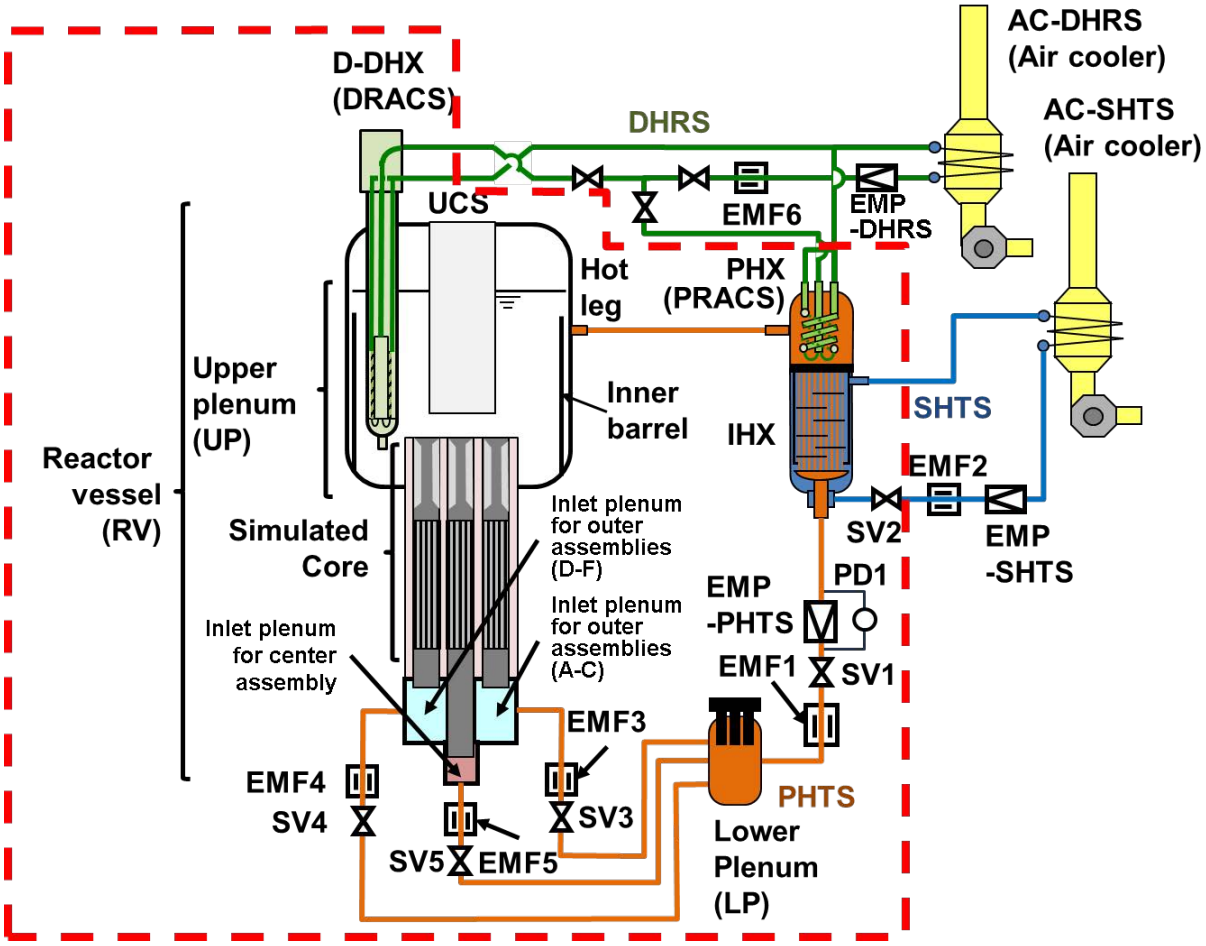


**Figure 2 Flow diagram of PLANDTL-DHX.**
**(The area surrounded by the red dotted line corresponds to the area for benchmark analysis)**

### 2.2 Reactor Vessel (RV)

#### 2.2.1 Upper Plenum of the RV (UP-RV)

Figures 3 and 4 show the dimensions of the UP-RV on the vertical and horizontal cross-sections from the top view, respectively. Table 2 lists the major specifications of the UP-RV. The UP-RV was a cylindrical vessel with an inner diameter of 2.0 m and a height of 3.25 m. The UP-RV included the D-DHX equipped with coiled heat transfer tubes for DRACS, the inner vessel, and the upper core structure (UCS) above the core outlet. An outlet nozzle installed on the RV wall was located on the opposite side of the D-DHX. The inner vessel was installed for the thermal shield to the outer wall of the RV and mitigation of the circumferential effect of the drifting flow to the outlet nozzle. The UCS was a vacant cylindrical structure filled with argon gas. Three thermocouple-trees, which had thermo-couples in a tree-like configuration, were installed at 315$^{o}$ near the D-DHX (TC-1), 30$^{o}$ (TC-2), and 150$^{o}$ (TC-3), respectively, at 500 mm from the center.

Figure 5 shows the configuration of the structures around the upper part of the simulated core in the UP-RV. The upper part of the simulated core was partially inserted in the UP-RV, as shown in Fig.3. In the inserted part, three cylindrical structures were installed with an upper cover plate for thermal shielding to the simulated core to prevent thermal interaction from the UP-RV.

#### 2.2.2 Simulated Core

Figures 6 (a) and (b) illustrate the cross-sectional view of the simulated core with 7 assemblies and an overview of the 37-pin bundle of the center assembly, respectively. The simulated core consisted of the center assembly with 37 electric heater pins and six outer assemblies with 7 electric heater pins with a larger diameter. Each heater pin had a wire spacer to simulate the fuel pin of a large-scale SFR. The simulated core was partially inserted and connected to the UP-RV, as shown in Fig. 3. The center assembly was a partial model of a fuel assembly of the SFR. The axial layout of the bundle region of the simulated core represents a full-scale model of the fuel assembly of the SFR.

Figure 7 shows the dimensions of the simulated core on the horizontal cross-section. In the simulated core, a corrugated duct (outer duct) to form the outer boundary of the core was installed in the outer shell. Inside the outer duct, the IWG around the wrapper tube was formulated.

Figures 8 (a) and (b) show the axial location of the convection suppression plates in the core region and horizontal views of the shapes of the plates. The convection suppression plates were installed between the outer shell and the outer duct to make sodium stagnant.

Figure 9 shows the dimensions of the inlet part of the simulated core with the center and outer assemblies. As for the inlet part of the simulated core, three inlet flow paths were manufactured: the center path from Inlet-A brought the flow from the bottom of the core section to the center assembly, and the other two paths from Inlet-B and Inlet-C brought the flow to three outer assemblies for A to C and D to F, respectively.

Figures 10 (a) and (b) show the dimensions of the center and outer assemblies, respectively. Each assembly was divided into four regions; the lower non-heated section, heated section, upper non-heated section, and neutron shield section. Table 3 lists the major specifications of assemblies in the simulated core. The center assembly is composed of 37 electric heater pins, a wire spacer at each pin (not shown in the figure), a neutron shield section, and a hexagonal wrapper tube, as shown in Fig. 10. Regarding the center assembly, the pin diameter, the pin pitch, the diameter of wire spacer, and the wire winding pitch

were almost the same as those of the core fuel assembly in the SFR.

Figure 11 shows the locations of the starting positions of the wire spacer around the pin. The starting position was common for all pins. The wrapper tube of each assembly was made of stainless-steel 304 (SS304) with a thickness of 4 mm. Instead of the pad-type spacer, 50 mm long round rods with a diameter of 7 mm were welded in the vertical-long direction on the outer surfaces at the center of the wrapper tube at two axial locations to maintain an IWG width of 7 mm between assemblies around the center assembly. In addition, 50 mm long round rods with a diameter of 3 mm were welded on the outer surfaces of the outer assemblies as the spacer to keep the flow path through the gap between the assembly and the outer duct (see Fig. 7).

Figures 12 and 13 show the axial distributions of linear power density ($q$) normalized by the maximum value at the peak of the profile ($q_{\mathrm{peak}}$) for the center 37-pin and outer 7-pin bundle, respectively. The bottom of the lower non-heated section was set at $z$ = 0 mm. Electric lead wire made of nickel and copper was installed in a lower non-heated section with weak induction heat.

### 2.2.3 Lower Plenum (LP)

Figure 14 shows the dimensions of the LP. In the SFR, low-temperature sodium through the cold-leg of the PHTS enters the LP of the RV after exchanging the heat with sodium at the IHX in the SHTS. In PLANDTL-DHX, the LP was placed separately from the RV, as shown in Fig. 2 and modeled with a 2.4 m high cylindrical vessel with an inner diameter of 0.8 m with an ellipsoidal dished head on the lower side. The vessel was made of stainless-steel 316 (SS316). In the vessel, 21 electric heaters with a capacity of 56 kW were installed from the top plate to control the inlet temperature. The bottom end plates of the inner cylinder, outlet guide plate, and LP were in semi-elliptic shape (with a one-fourth depth of the diameter). Sodium flows to the simulated core through the three independent inlet pipes: one connected to the center assembly, and the other two connected to the three outer assemblies A, B, and C, and D, E, and F, respectively, as shown in Fig. 9. The distributed flowrates to the assemblies were regulated at the nozzles in the piping.

**Table 2 Major specifications of UP-RV.**

| Item | | Unit | Value |
|---|---|---|---|
| Height | | m | 3.25 |
| Inner diameter | | m | 2.0 |
| Thickness of RV | | m | 0.02 |
| Normal sodium level from the bottom of UP-RV | | m | 2.01 |
| Sodium volume at normal sodium level in UP-RV | | $m^3$ | 5.7 |
| Ellipsoidal dished head (Top and bottom) | Inner diameter | m | 2.0 |
| | Height | m | 0.563 |

**Table 3 Major specifications of assemblies in the simulated core.**

| Components | Item | Unit | Center assembly | Outer assembly |
|---|---|---|---|---|
| Assembly | Number | - | 1 | 6 |
| | Outer flat-to-flat distance of assembly | m | 0.071 | 0.071 |
| | Inner flat-to-flat distance of assembly | m | 0.063 | 0.063 |
| | Wrapper tube thickness | m | 0.004 | 0.004 |
| | Assembly pitch | m | 0.078 | 0.078 |
| | IWG width at the center region | m | 0.007 | 0.007 |
| | IWG width at the peripheral region | m | 0.0035 | 0.0035 |
| Heater pin | Number | - | 37 | 7 |
| | Pin pitch | m | 0.0099 | 0.0224 |
| | Pin diameter | m | 0.0083 | 0.0208 |
| Spacer wire | Diameter | m | 0.0015 | 0.0015 |
| | Wire winding pitch | m | 0.165 | 0.165 |
| Coolant | Cross-sectional area | $m^2$ | 0.00137 | 0.00105 |
| | Hydraulic diameter | m | 0.00404 | 0.00591 |

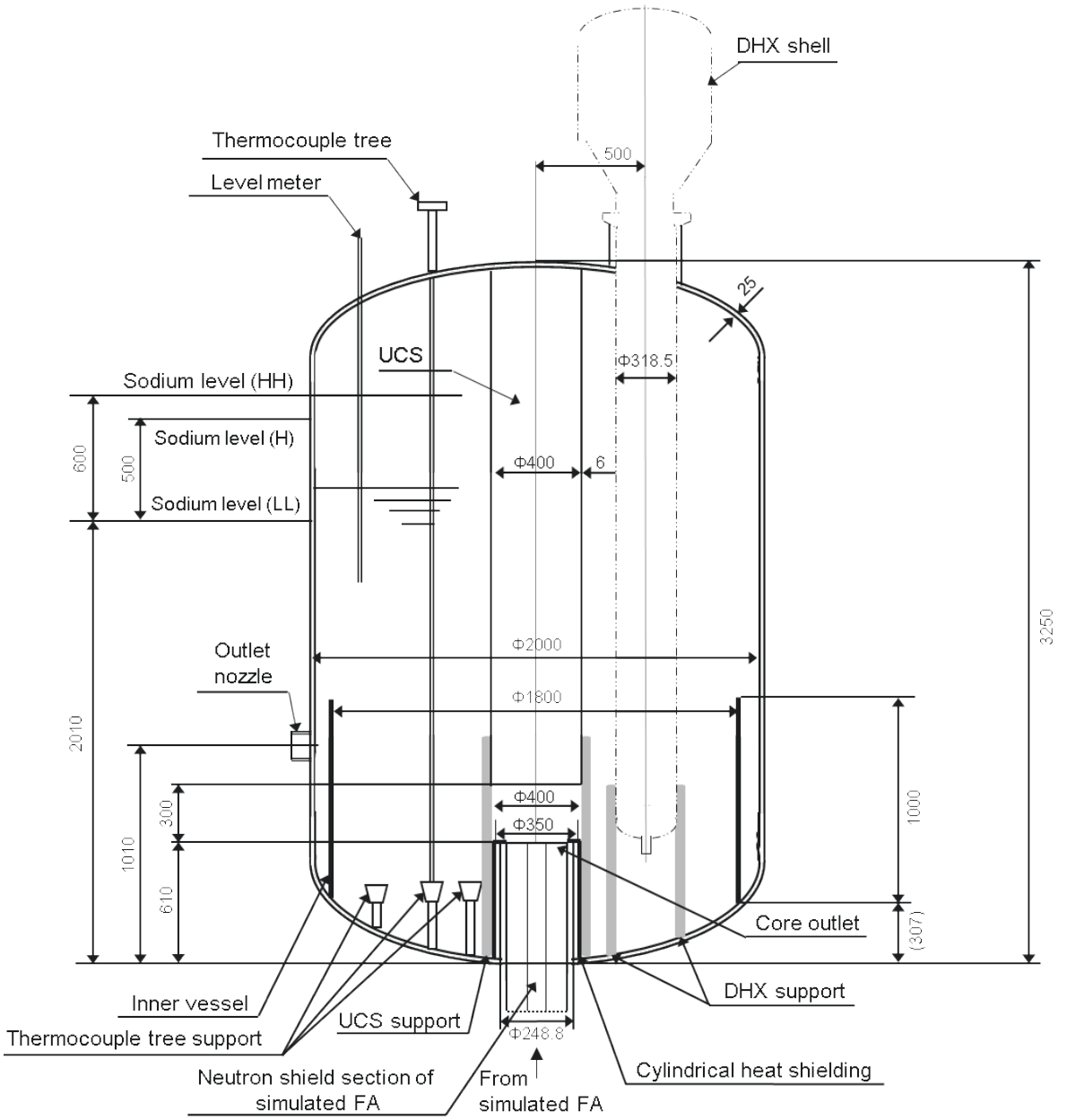


(Unit: mm)

**Figure 3 Dimensions of UP-RV on the vertical cross-section.**

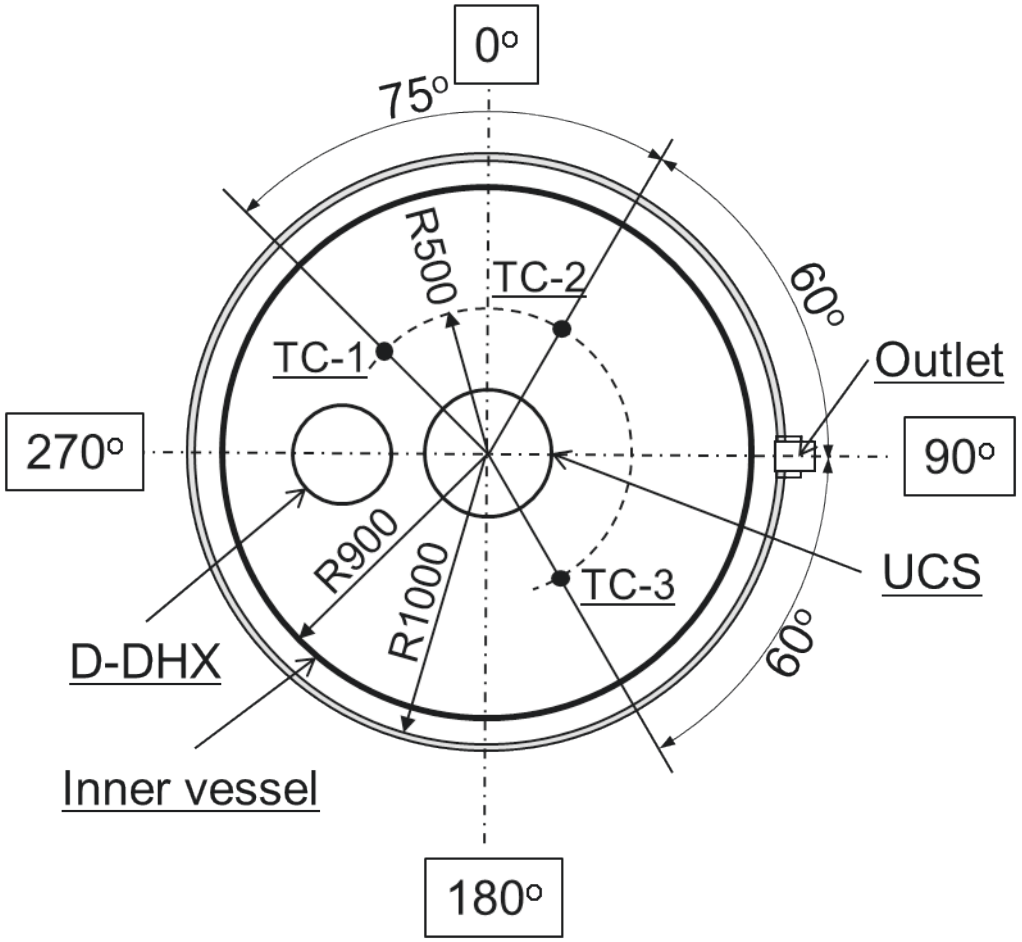


(Unit: mm)

**Figure 4 Dimensions of UP-RV on the horizontal cross-section from the top view.**

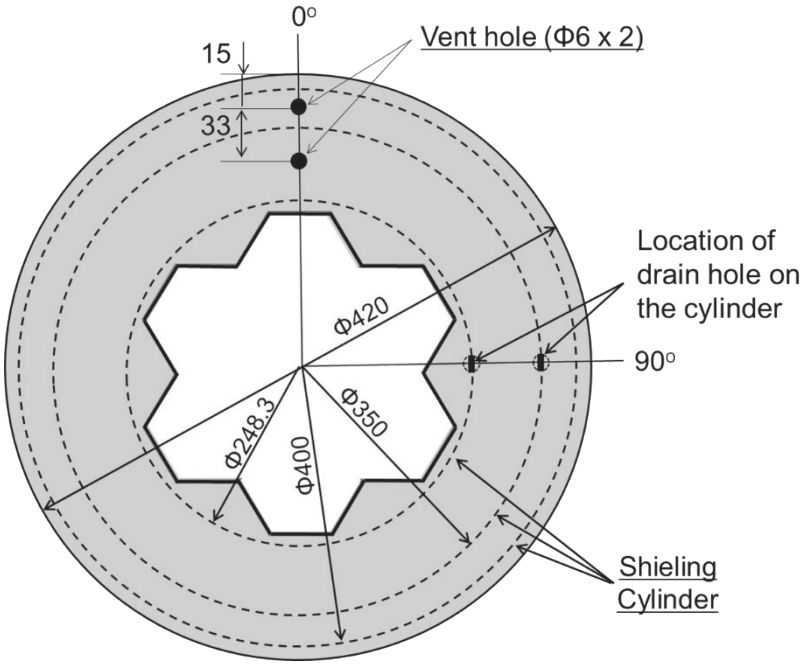


**(a) Upper cover plate (plate thickness: 6 mm)**

(Unit: mm)

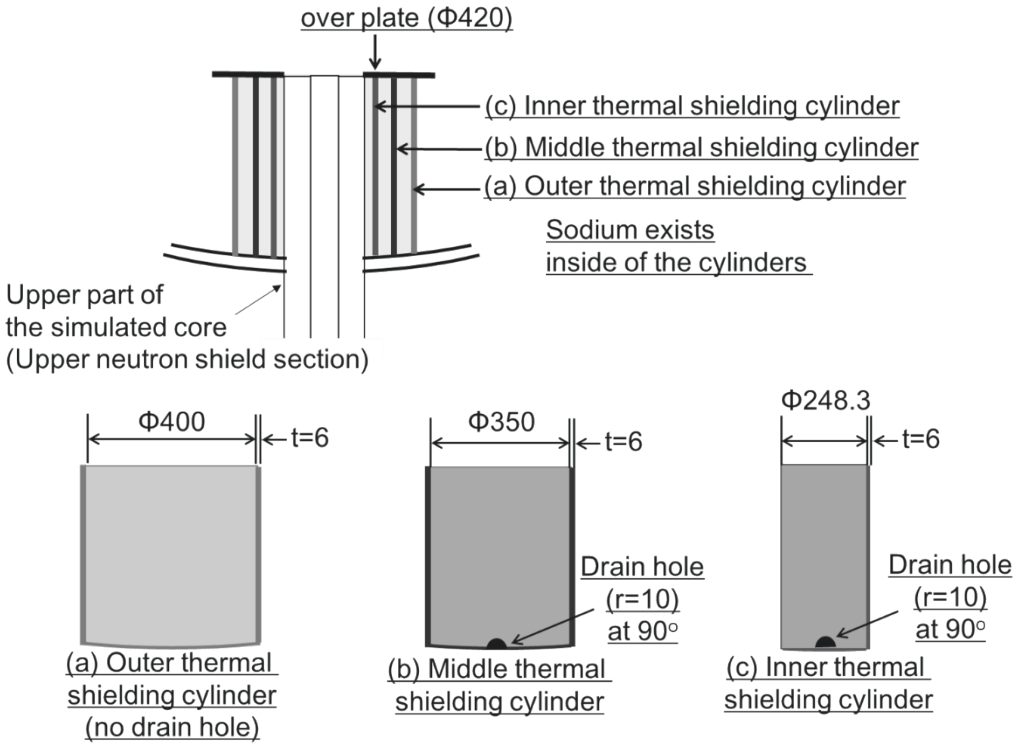


**(b) Upper structure**

**Figure 5 Configuration of structures around the upper part of the simulated core in UP-RV.**

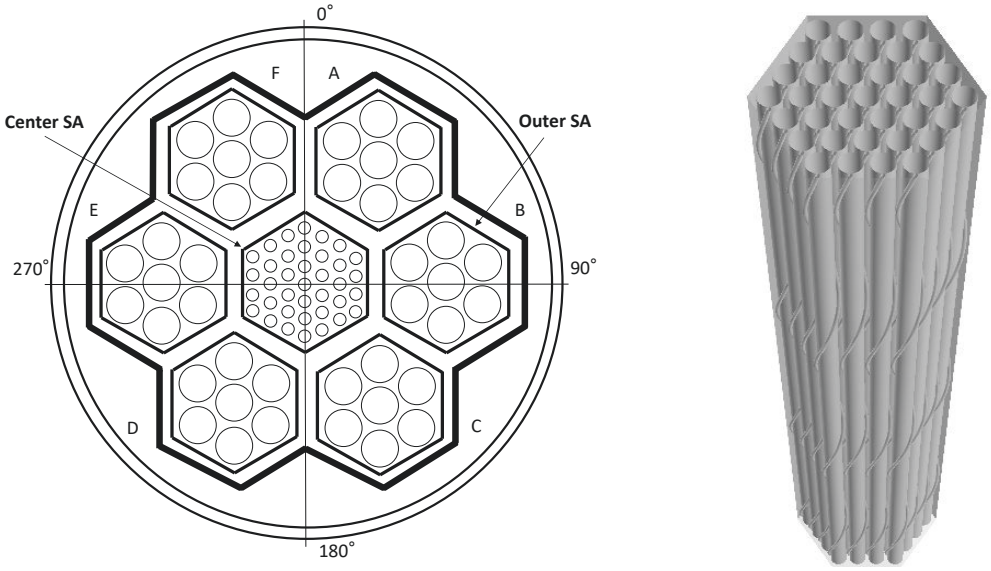


**(a) Cross section** **(b) Overview of center assembly**

**Figure 6 Outline of the simulated core.**

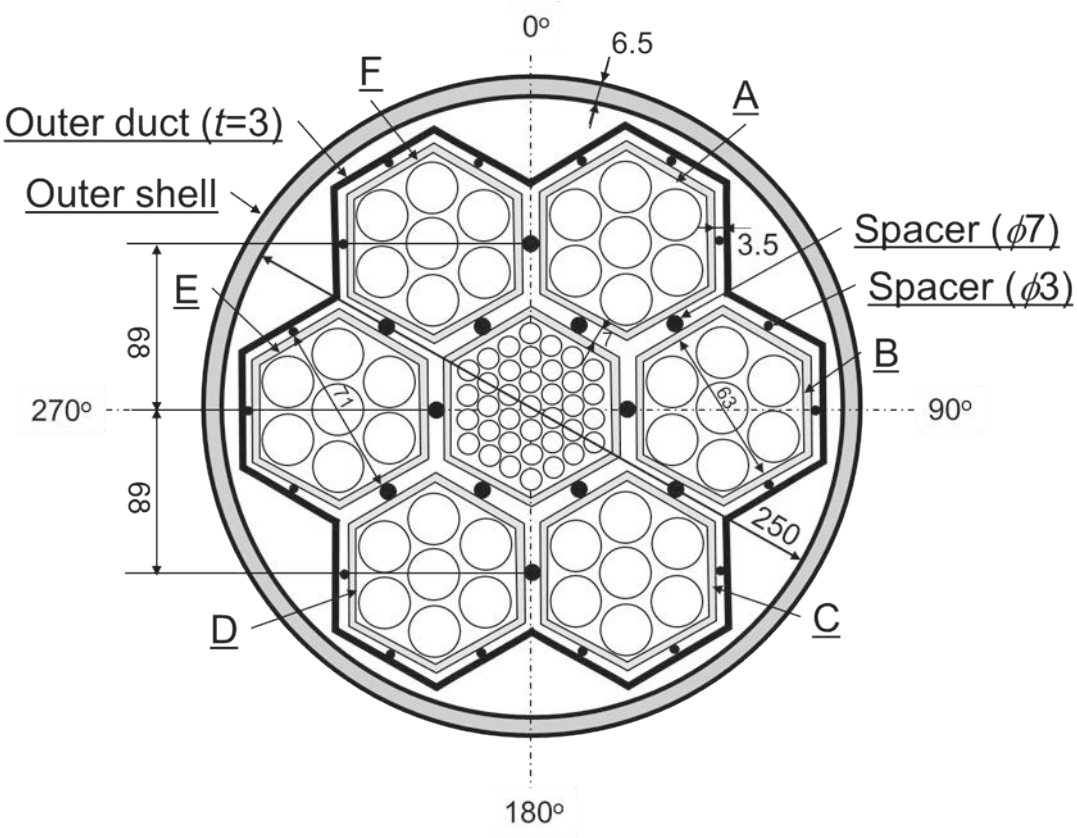


(Unit: mm)

**Figure 7 Dimensions of the simulated core on the horizontal cross-section.**
**(Wire spacers are not shown in the figures.)**

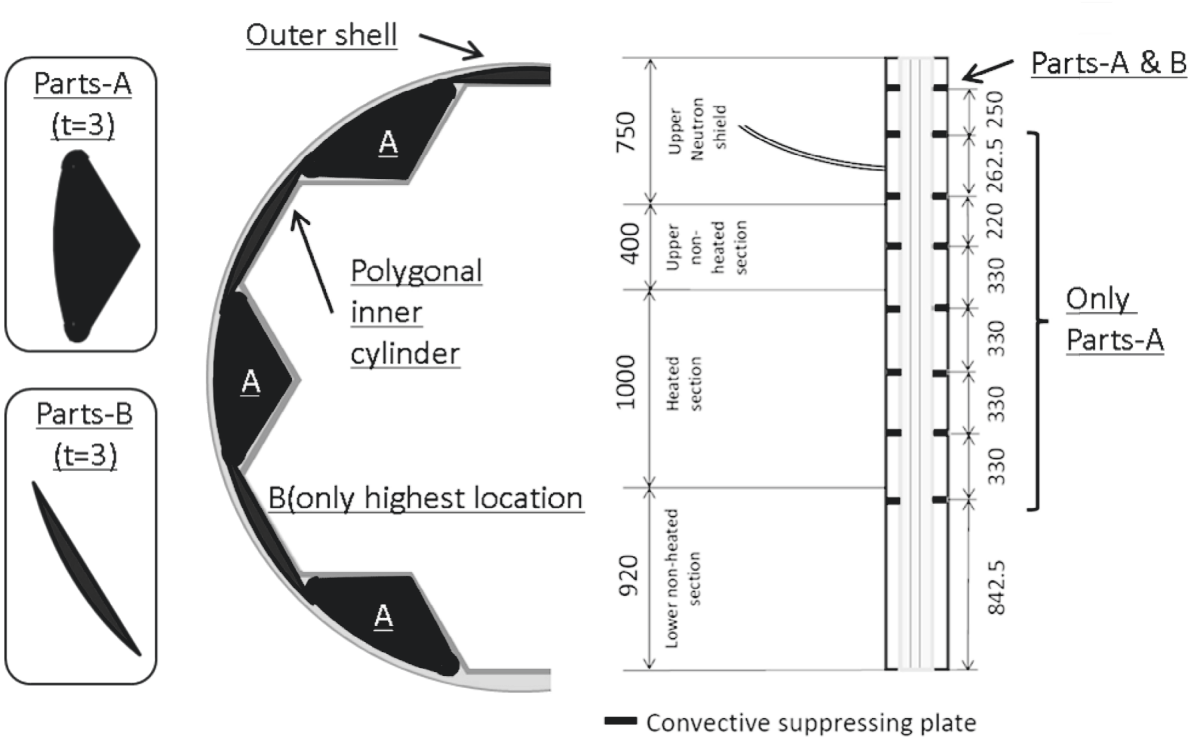


(Unit: mm)

**Figure 8 Configurations of convection suppression plates in the core region.**

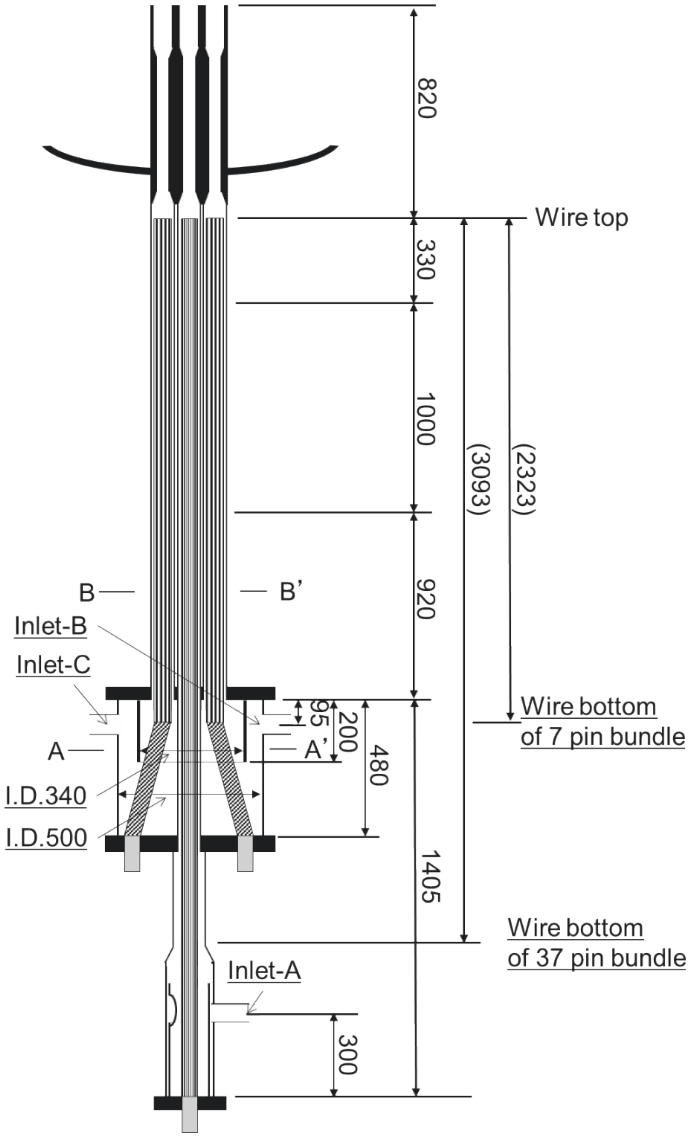


**(a) Overview**

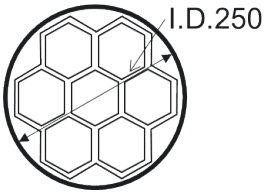


**(b) B-B' cross-section**

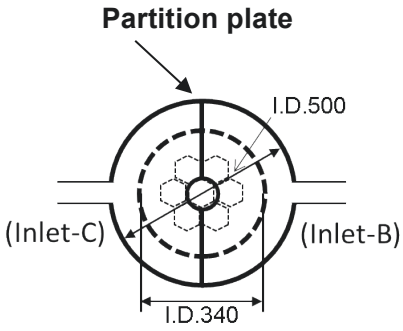


**(c) A-A' cross-section (Inlet-B for three outer assemblies of A, B, and C and Inlet-C for three outer assemblies of D, E, and F)**

(Unit: mm)

**Figure 9 Dimensions of the inlet part of the simulated core with center and outer assemblies.**

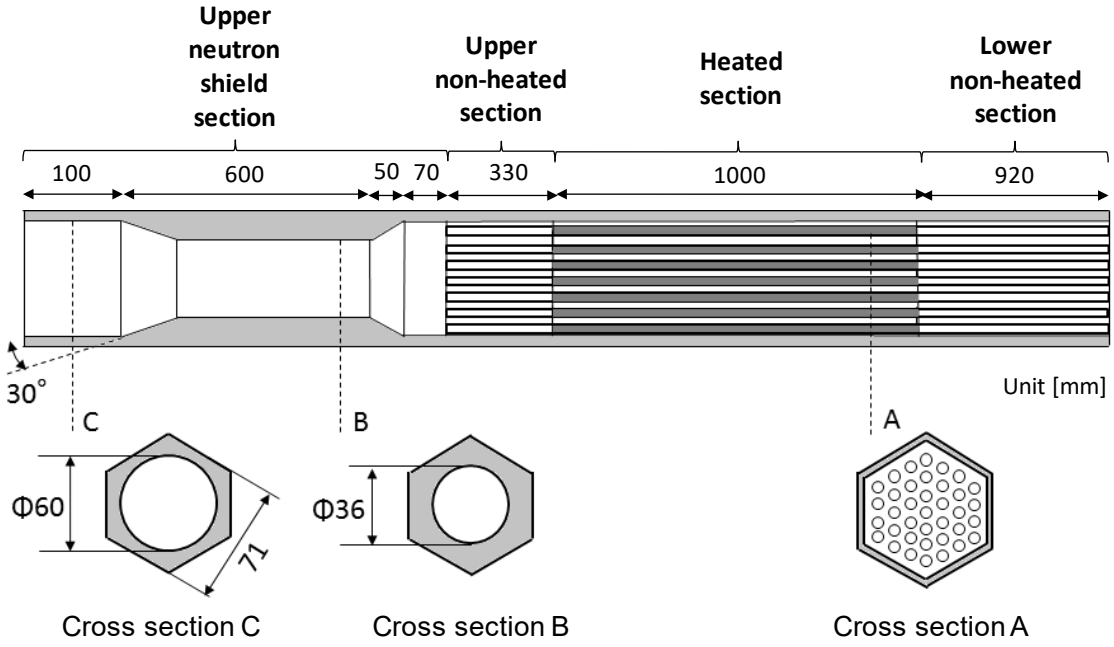


**(a) 37-pin bundle for center assembly**

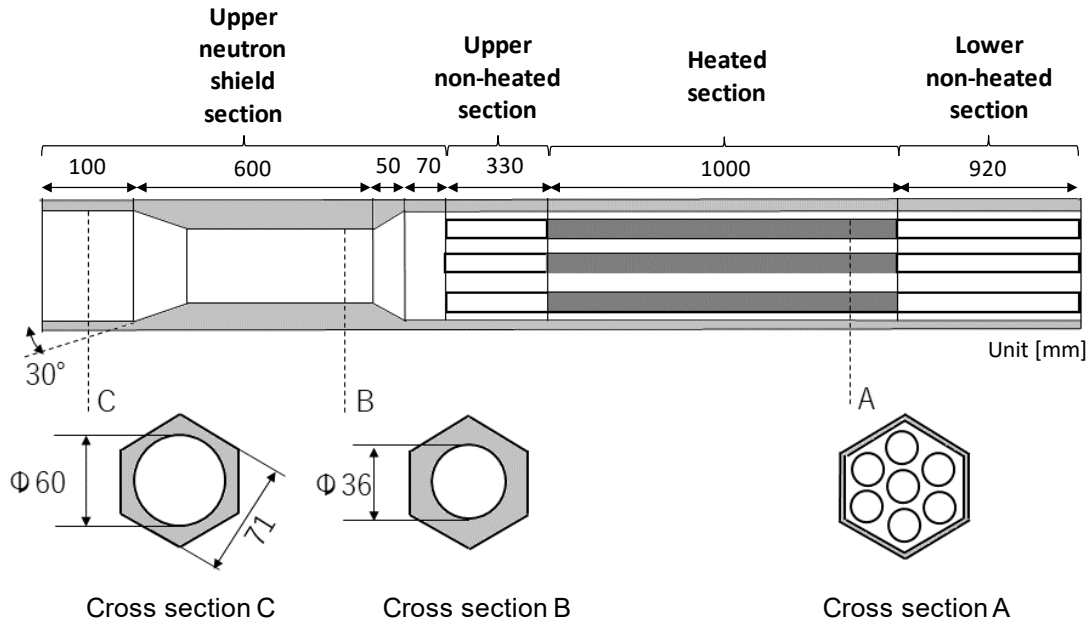


**(b) 7-pin bundle for outer assembly**

**Figure 10 Dimensions of center and outer assemblies.**
**(Wire spacers are not shown in the figures.)**

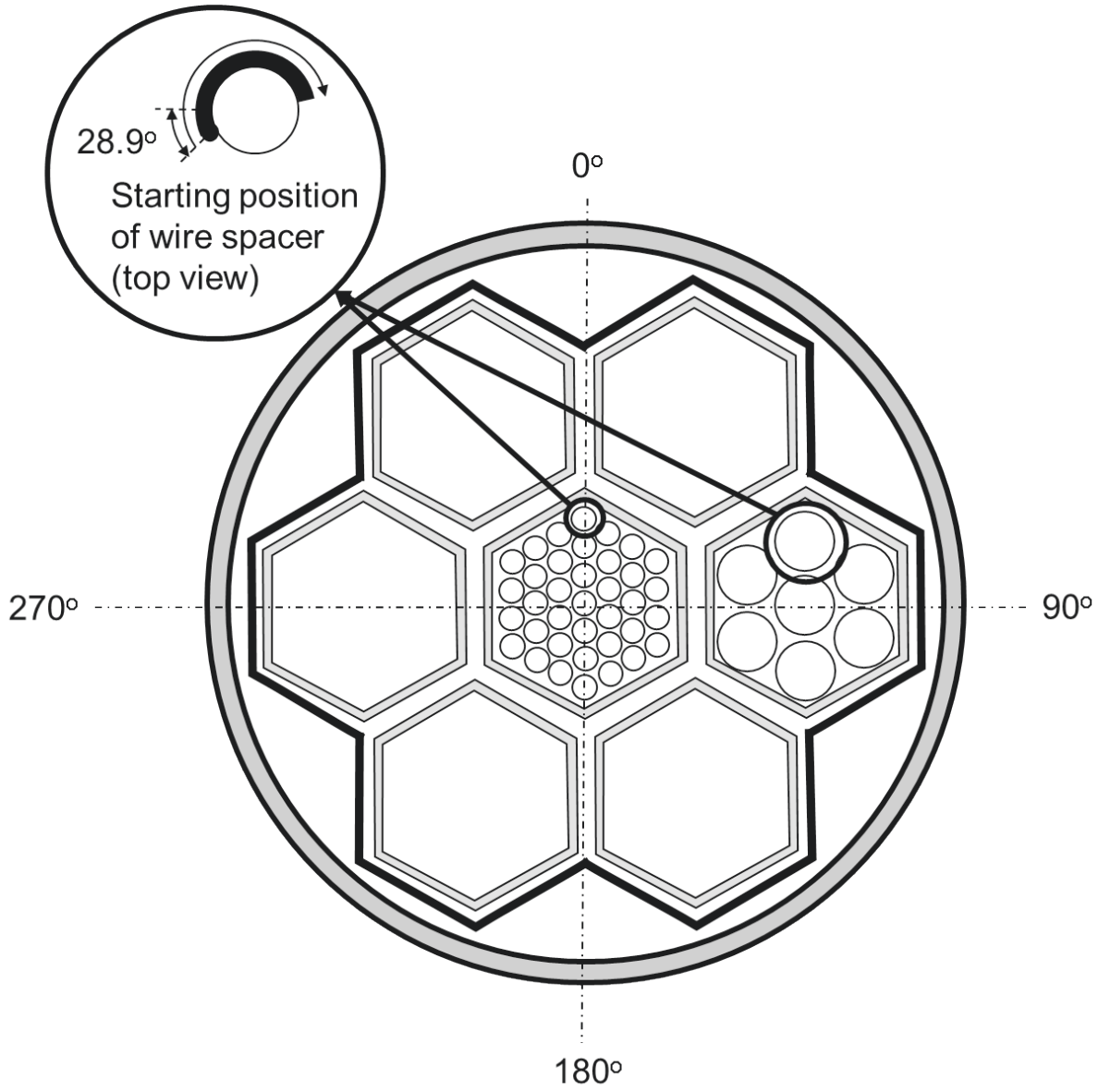


**Figure 11 Locations of starting positions of wire spacer around the pin.**

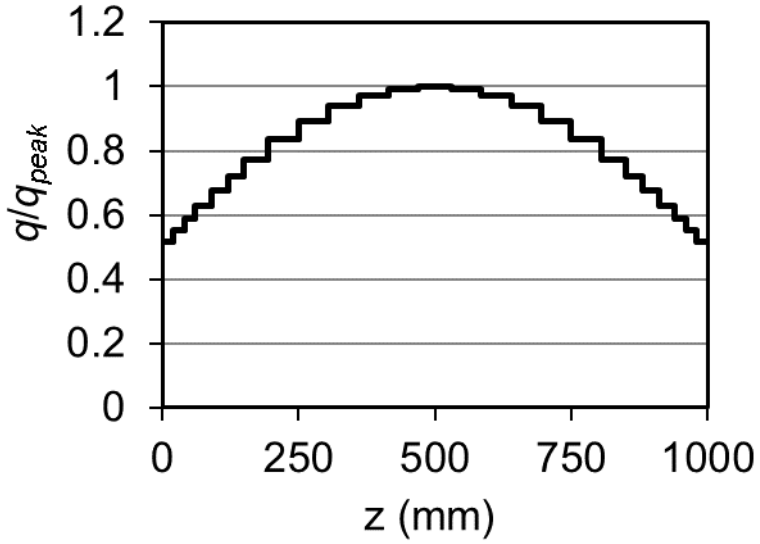


**Figure 12 Axial distribution of normalized power density in the heated section for the center 37-pin bundle.**

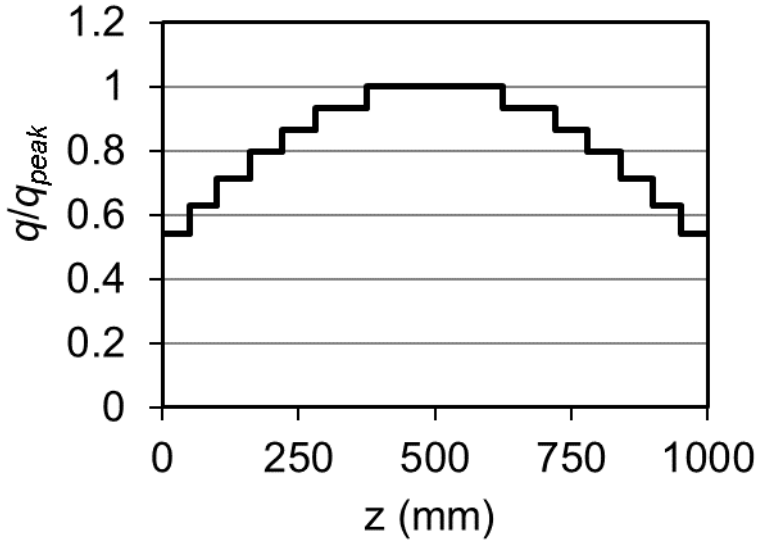


**Figure 13 Axial distribution of normalized power density in the heated section for the outer 7-pin bundle.**

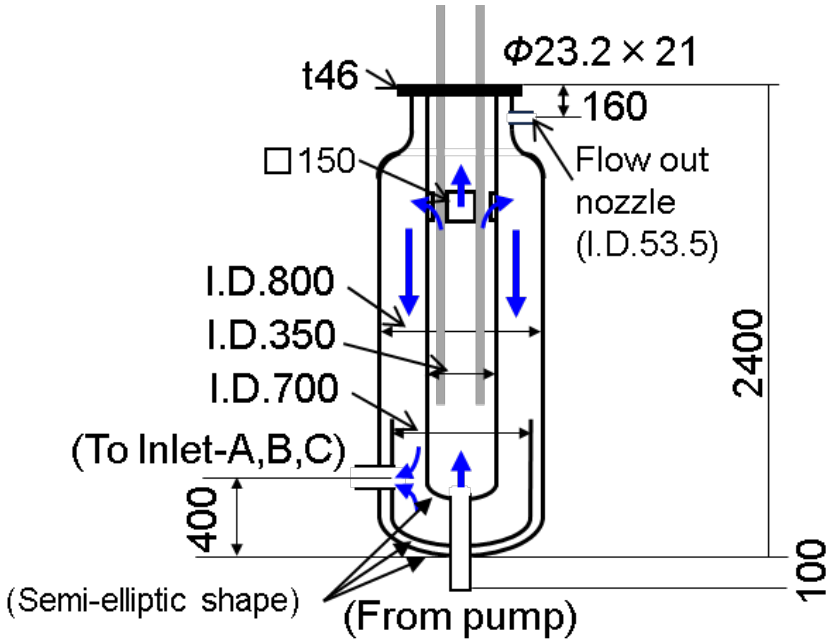


(Unit: mm)

**(a) Vertical cross-section**

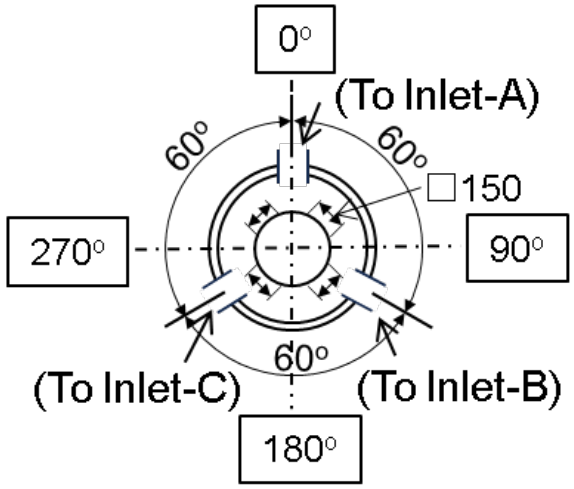


(Unit: mm)

**(b) Horizontal cross-section viewed from the top of the vessel**

**Figure 14 Dimensions of LP.**

### 2.3 Primary Heat Transport System (PHTS)

Figure 15 shows the layout of major components and piping in the PHTS. Points to show floor level are located at corners where the angle of piping is changed from horizontal to vertical one or vertical to horizontal one. Sodium heated in the core flowed out from the UP-RV and went to the IHX through the hot-leg piping (red line) of the PHTS. Heat in the PHTS was transferred to the SHTS through the heat transfer straight tubes in the IHX, and the temperature of the sodium in the PHTS was decreased. The sodium at low temperatures in the cold-leg piping (blue line) of the PHTS to the LP was pumped up by EMP-PHTS (EMP101) and went to the LP through the SV1 (SV101M) flow control valve and EMF1 (EMF101). From the LP, the sodium went to the core section through three pipelines to Inlet-A, Inlet-B, and Inlet-C. The pipeline to Inlet-A (light brown line) was connected to the center assembly through the two valves, SV5 (SV105M) and SV5a (SV105A), and a flowmeter, EMF5 (EMF105). Another pipeline to Inlet-B (dark brown line) was connected to one side-core region consisting of three outer assemblies of A, B, and C via the SV3 (SV103M) valve and the EMF3 (EMF103) flowmeter. The other pipeline to Inlet-C (dark brown line) was connected to the opposite side-core region consisting of another three outer assemblies of D, E, and F via the SV4 (SV104M) valve and the EMF4 (EMF104) flowmeter. The pipe diameter of the PHTS from the RV outlet to the LP inlets was 4 inches and those from the LP outlet to the core inlets were 2 inches. Table 4 lists the specifications of piping in the PHTS. Figure 16 shows the elevations of components in the PHTS of PLANDTL-DHX. Table 5 lists the major specifications of EMP in the PHTS (EMP-PHTS).

**Table 4 Major specifications of piping in PHTS.**

| Section | | | Inner diameter (m) | Length (m) | Number of elbows | Number of valves |
|---|---|---|---|---|---|---|
| RV (outlet) | - | IHX (inlet) | 0.1063 (4 inches) | 12.05 | 7 | 0 |
| IHX (outlet) | - | LP (inlet) | 0.1063 (4 inches) | 33.77 | 16 | 1 |
| LP (outlet) | - | RV (inlet-A) | 0.0535 (2 inches) | 11.67 | 8 | 2 |
| LP (outlet) | - | RV (inlet-B) | 0.1063 (4 inches) | 12.58 | 6 | 1 |
| | | | 0.0535 (2 inches) | 2.59 | 2 | 0 |
| LP (outlet) | - | RV(inlet-C) | 0.1063 (4 inches) | 12.58 | 6 | 1 |
| | | | 0.0535 (2 inches) | 2.59 | 2 | 0 |

**Table 5 Major specifications of EMP-PHTS (EMP101).**

| Type | Unit | Annular Linear Induction Pump (ALIP) |
|---|---|---|
| Flow range (maximum) | t/h | 54 |
| Maximum operating temperature | $^{o}$C | 625 |
| Maximum operating pressure | $10^3$ kg/m$^2$G | 80 |

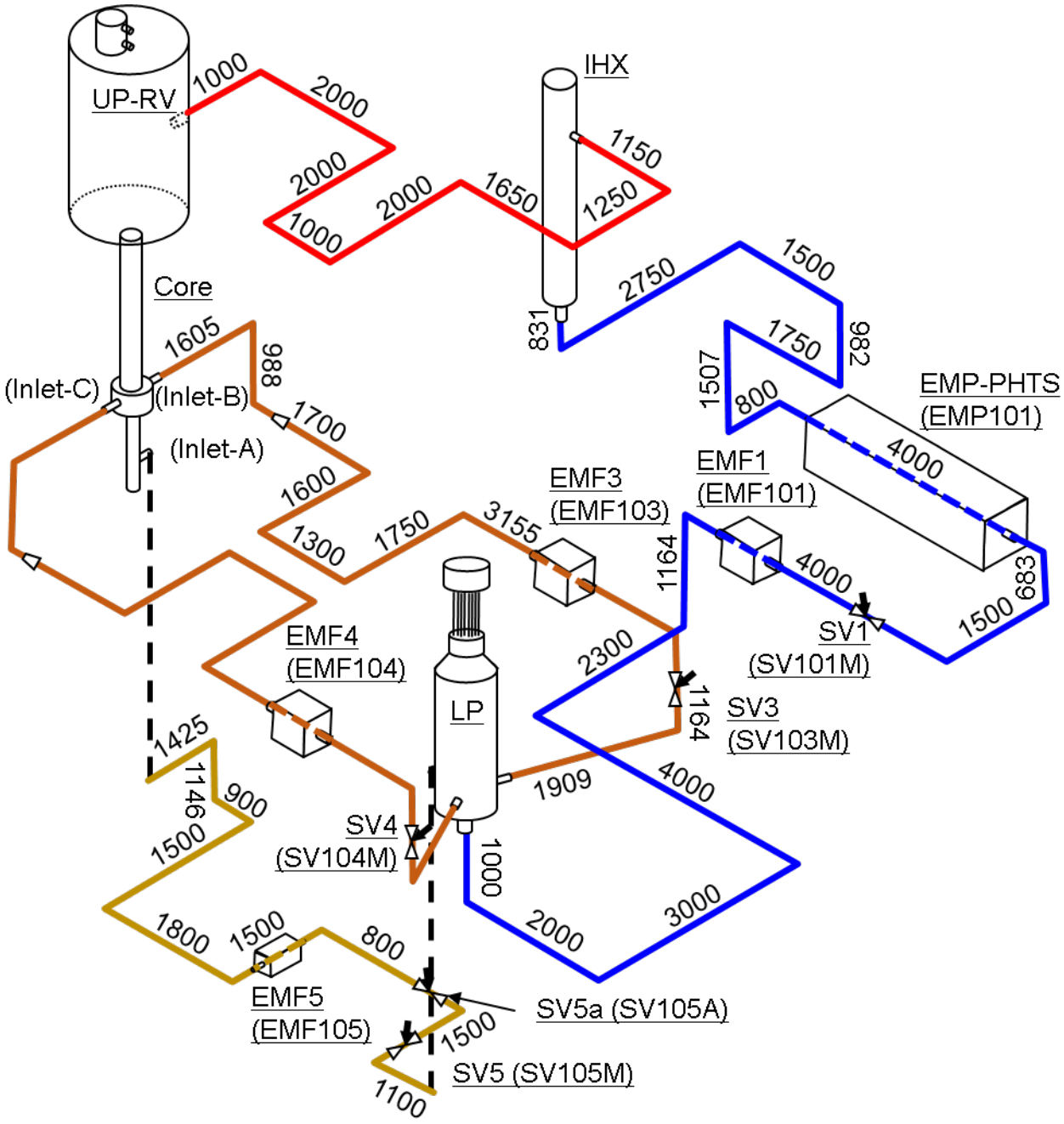


(Unit: mm)

**Figure 15 Layout and specifications of major components and piping in the PHTS.**

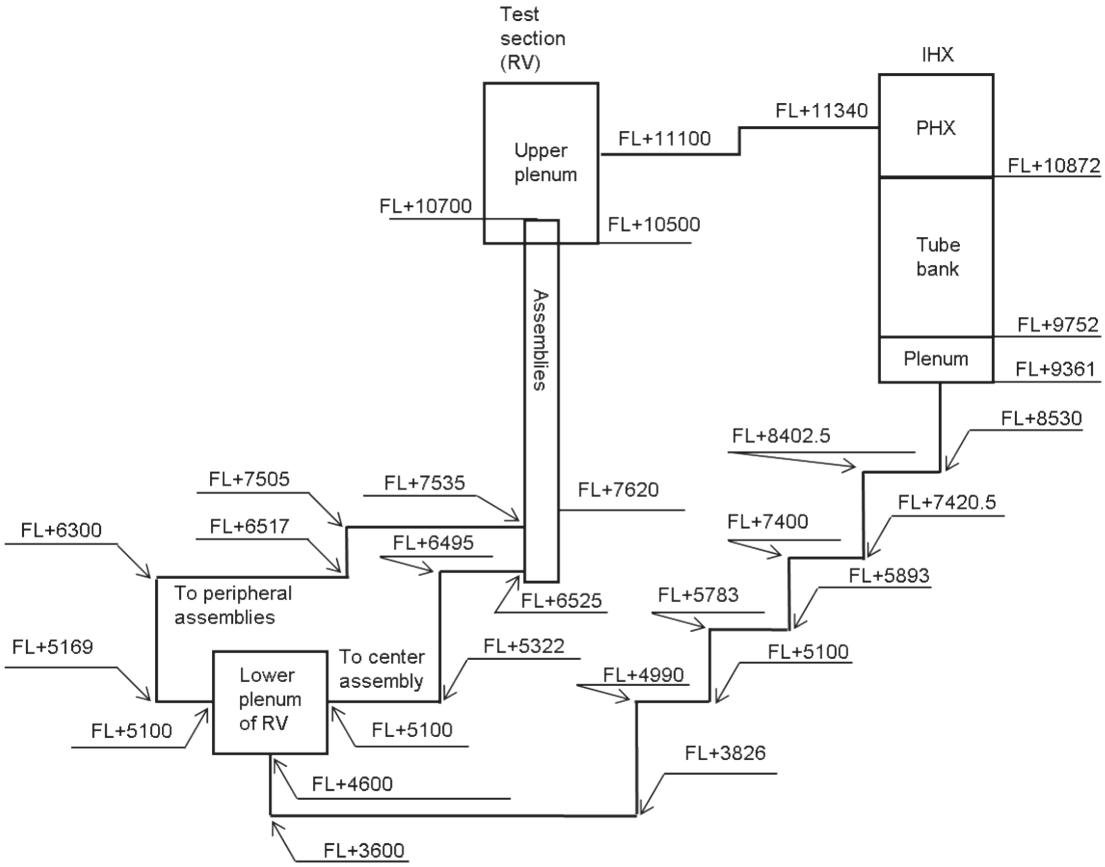


(Unit: mm)

**Figure 16 Elevations of components in the PHTS of PLANDTL-DHX.**

### 2.4 Intermediate Heat Exchanger (IHX)

Figure 17 shows the dimensions and structure of the IHX and baffle plates located in the tube bank. The IHX was a shell-and-tube type heat exchanger with straight heat transfer tubes. In the PHTS, the sodium entered from the entrance windows on the shell in the UP-IHX flowed down to the LP at the bottom of the IHX through the straight heat transfer tubes and flowed out to the cold-leg of the PHTS. Sodium in the SHTS entered from the lower inlet nozzle and flowed out of the outlet nozzle on the shell at the middle of the IHX after flowing through the outside of the heat transfer tubes. In the UP-IHX, a heat exchanger for the PRACS (i.e., PHX) consisting of two helical tubes was installed (shown by the area in the red dotted line). The tube bank for the IHX was composed of 145 straight tubes with an inner diameter of 23 mm and a pitch length between neighboring tube centers of 32 mm. As shown in Fig. 17(c), 6 baffle plates were installed in the tube bank to support the tubes and promote thermal mixing. In each baffle plate, a segment including 2 tubes for heat transfer and a tie-rod on the line from 90 º to 270 º was cut off to formulate a zigzag flow of the primary coolant in the tube bank. Table 6 shows the major specifications of the IHX.

**Table 6 Major specifications of heat transfer tubes in the IHX.**

| Item | Unit | Value |
|---|---|---|
| Type of heat transfer tubes | - | Straight |
| Arrangement of tubes | - | Equilateral triangle |
| Pitch of heat transfer tubes (center to center) | m | 0.032 |
| Inner diameter of heat transfer tube | m | 0.023 |
| Thickness of heat transfer tube wall | m | 0.0012 |
| Outer diameter of heat transfer tube | m | 0.0254 |
| Number of heat transfer tubes | - | 145 |
| Heat transfer area | $m^2$ | 9.25 |
| Heat transfer capacity | MW | 1.2 |

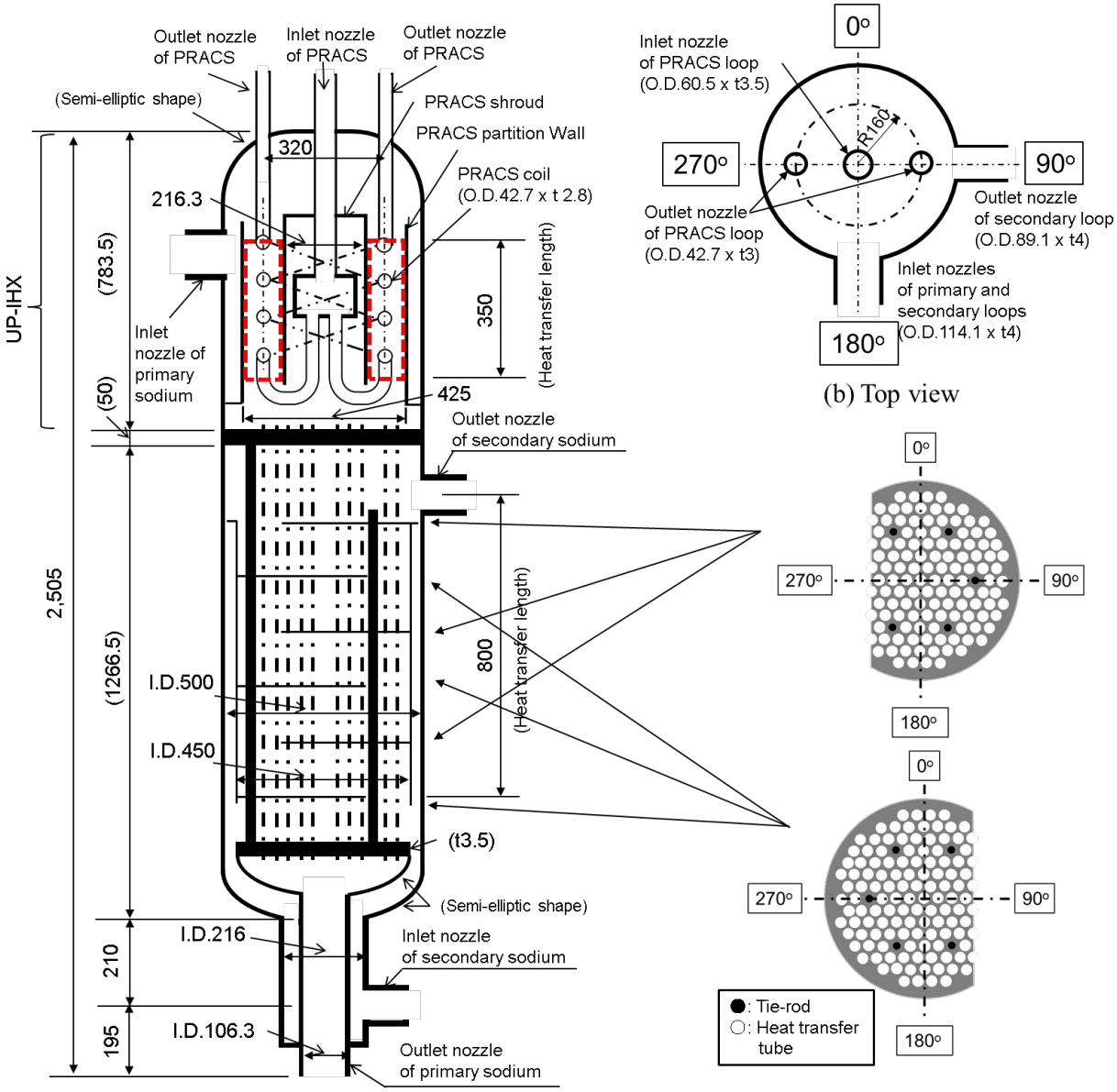


(Unit: mm)

**Figure 17 Dimensions and compositions of IHX and PHX for PRACS in the UP-IHX. (The square region of the red dotted line indicates the area of PHX for heat transfer)**

### 2.5 Secondary Heat Transport System (SHTS)

Table 7 lists the specifications of major components in the SHTS. In the SHTS, sodium at a high temperature from the IHX after exchanging heat with the sodium in the PHTS flowed to the AC-SHTS. From the AC-SHTS, sodium returned to the IHX inlet on the SHTS side driven by the EMP-SHTS through EMF2 and the SV2 sodium valve, as shown in Fig. 2. The diameter of the piping for the SHTS was 4 inches while the diameter at the inlet and outlet nozzles of the IHX was 3 inches. Table 8 lists the major specifications of the EMP-SHTS. Table 9 lists the major specifications of the AC-SHTS, which was the final heat sink. In the AC-SHTS, sodium flowed within the tubes, while air flowed through the area outside the tubes. The AC-SHTS has sufficient capacity to remove heat from the core and auxiliary sodium heaters equipped in the PHTS.

Components and piping in the SHTS are not within the scope of the present benchmark analysis.

**Table 7 Specifications of major components in SHTS**

| Item | Unit | Value |
|---|---|---|
| AC-SHTS (maximum capacity) | MW | 1.72 |
| EMF2 measurement range | liter/min | 0 - 700 |
| SV in the SHTS (SV2) | - | Needle valve (see Table 15) |

**Table 8 Major specifications of EMP-SHTS.**

| Item | Unit | Value |
|---|---|---|
| Type | - | Annular Linear Induction Pump (ALIP) |
| Flow range (maximum output) | kg/s (liter/min) | 7.53 (560) |
| Maximum operating temperature | $^{o}$C | 625 |
| Maximum operating pressure | $10^3$ kg/m$^2$G | 80 |

**Table 9 Major specifications of AC-SHTS.**

| Item | Unit | Value |
|---|---|---|
| Type of heat transfer tube | - | Multi-layered tube with fins |
| Heat transfer area | m$^2$ | 11.1 |
| Heat exchange capacity | kW | 1,720 |
| Maximum operating temperature | $^{o}$C | 625 |
| Maximum operating pressure | $10^3$ kg/m$^2$G | 80 |

## 2.6 Decay Heat Removal System (DHRS)

### 2.6.1 Components and Piping

See Fig. 2 for the layout of the DHRS. Table 10 lists the major components of the DHRS. The DHRS had sodium valves to select the flow line through either of the two heat exchangers: D-DHX located in the UP-RV for DRACS and PHX in UP-IHX for PRACS. EMP-DHRS, EMF6, and AC-DHRS were commonly used for both flows. The diameter of the piping for the DHRS was 2 inches. In the test, either the D-DHX or the PHX was selected for the heat exchangers of the DHRS. In the DHRS, the sodium heated in the selected heat exchanger (D-DHX or PHX) flowed to the AC-DHRS and was cooled by exchanging the heat with the atmosphere. The cold sodium was pumped up by the EMP-DHRS and back to the selected heat exchanger through the EMF-DHRS and the sodium valves. Table 11 lists the major specifications of the EMP-DHRS. In the DHRS, the EMP-DHRS with a capacity of $1.667\times10^{-3}$ $m^3/s$ (100 liter/min) in maximum discharge flowrate was used. Table 12 lists the major specifications of the AC-DHRS. Sodium flowed inside of the tubes and air flowed through the area outside the tube bank. The AC-DHRS has sufficient capacity to remove the heat from the core and auxiliary sodium heaters equipped in the PHTS.

While components and piping in the DHRS are not within the scope of the present benchmark analysis, the two heat exchangers, D-DHX and PHX are, as shown in Fig. 2.

### 2.6.2 Direct Reactor Auxiliary Cooling System (DRACS)

Figure 18 shows the dimensions of the D-DHX installed in the UP-RV for the DRACS. The heat exchanger was a shell-and-tube-type heat exchanger with helical coils. Figure 19 shows the dimensions of the D-DHX in the vertical and horizontal cross-sections. Table 13 lists the major specifications of the D-DHX. The D-DHX installed in the UP-RV removed the decay heat directly from the core. The sodium from the AC-DHRS flowed down through the pipe to the header located in sodium and separated into five tubes in the inner shroud. At the bottom of the D-DHX, the direction of the sodium flow turned from downward to upward through the five helical coils., Sodium in the UP-RV entered the D-DHX from the 4 square windows and flowed out from the outlet nozzle at the bottom of the D-DHX, exchanging the heat of the sodium in the UP-RV with that in the DHRS. The four square windows on the primary side were 110 mm on each side at intervals of 90°, and thermocouples were set at 0° and 90°.

### 2.6.3 Primary Reactor Auxiliary Cooling System (PRACS)

Table 14 lists the major specifications of the PHX for PRACS. As shown in Fig. 17, the PHX for PRACS (shown by the area in red colored dotted-line) was installed in the UP-IHX. The PHX had two helical coils. The AC-DHRS was commonly used in both PRACS and DRACS.

**Table 10 Major components of DHRS**

| Item | Unit | Value |
|---|---|---|
| EMF | $10^{-3}$ $m^3/s$ | -0.833 ~ 1.667 |
| AC-DHRS (Max. capacity) | kW | 760 |
| D-DHX (DRACS) (Max. capacity) | kW | 130 |
| PHX (PRACS) (Max. capacity) | kW | 130 |

**Table 11 Major specifications of EMP-DHRS.**

| Item | Unit | Value |
|---|---|---|
| Type | - | Annular Linear Induction Pump (ALIP) |
| Maximum flowrate | $10^{-3}$ $m^3/s$ | 1.667 (100 (liter/min) |
| Maximum operating temperature | $^oC$ | 625 |
| Maximum operating pressure | $10^3$ $kg/m^2G$ | 80 |

**Table 12 Major specifications of AC-DHRS**

| Item | Unit | Value |
|---|---|---|
| Type | - | Multi-tube with fins |
| Heat transfer area | $m^2$ | 2.51 |
| Heat exchange capacity | MW | 0.76 |
| Maximum operating temperature | $^oC$ | 625 |
| Maximum operating pressure | $10^3$ $kg/m^2G$ | 80 |

**Table 13 Major specifications of D-DHX for DRACS.**

| Item | Unit | Value |
|---|---|---|
| Inner diameter of heat transfer tube | m | 0.015 |
| Wall thickness of heat transfer tube | m | 0.002 |
| Outer diameter of heat transfer tube | m | 0.019 |
| Number of heat transfer tubes | - | 5 |
| Inner diameter of shell | m | 0.2979 |
| Outer diameter of shroud | m | 0.1652 |
| Coil winding diameter | m | 0.244 |
| Degree of coil winding inclination | $^{o}$ (degree) | 20.1 |
| Height of heat transfer region | m | 0.729 |
| Length of the tube in the heat transfer region | m | 2.121 |
| Heat exchange capacity | MW | 0.13 |

**Table 14 Major specifications of heat transfer tubes in PHX for PRACS.**

| Item | Unit | Value |
|---|---|---|
| Inner diameter of heat transfer tube | m | 0.0427 |
| Wall thickness of heat transfer tube | m | 0.0028 |
| Outer diameter of heat transfer tube | m | 0.0371 |
| Number of heat transfer tubes | - | 2 |
| Coil winding diameter | m | 0.32 |
| Type of heat transfer tubes | - | Helical |
| Heat transfer area | $m^2$ | 0.66 |
| Heat exchange capacity | MW | 0.13 |

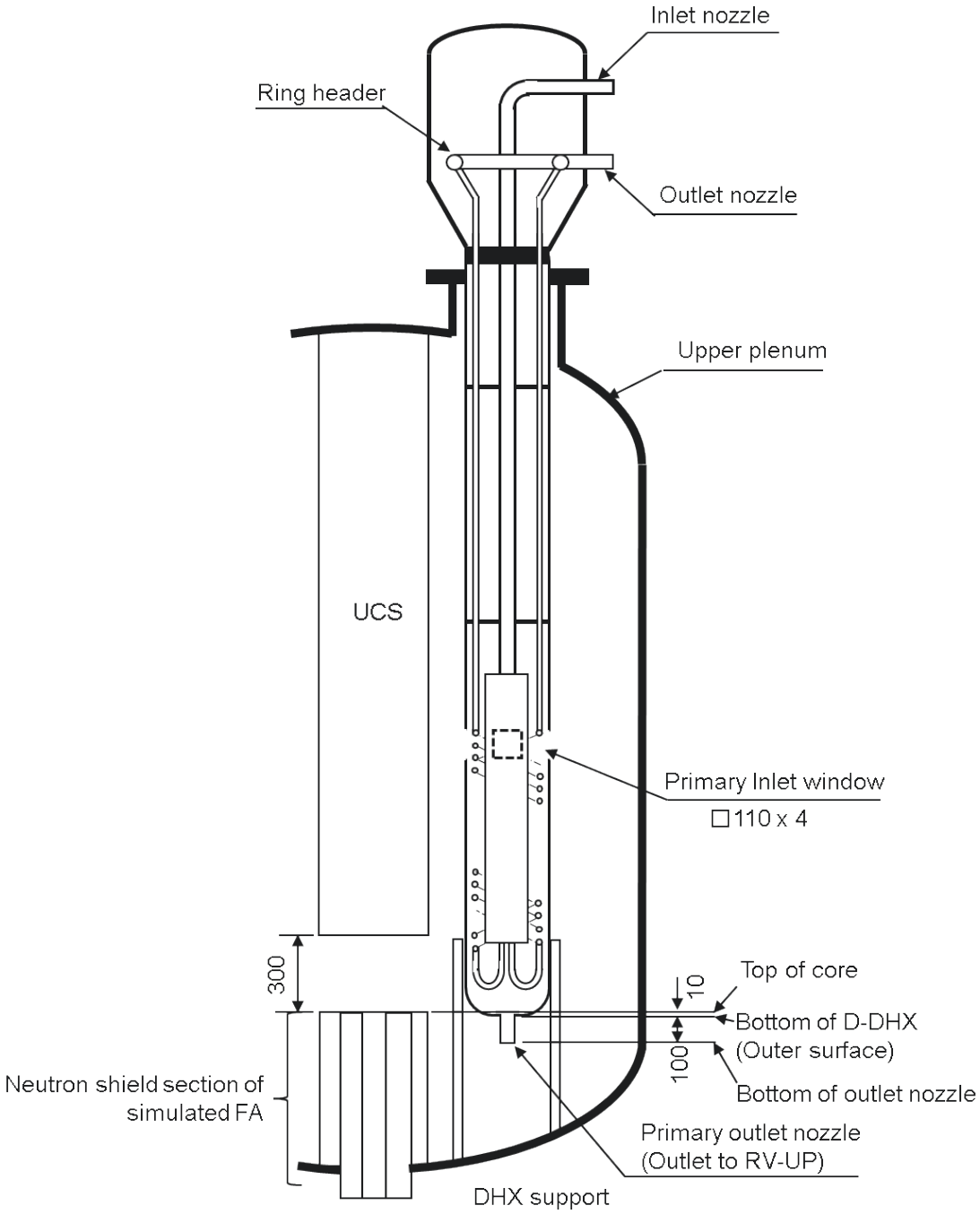


(Unit: mm)

**Figure 18 Location of D-DHX installed in UP-RV.**

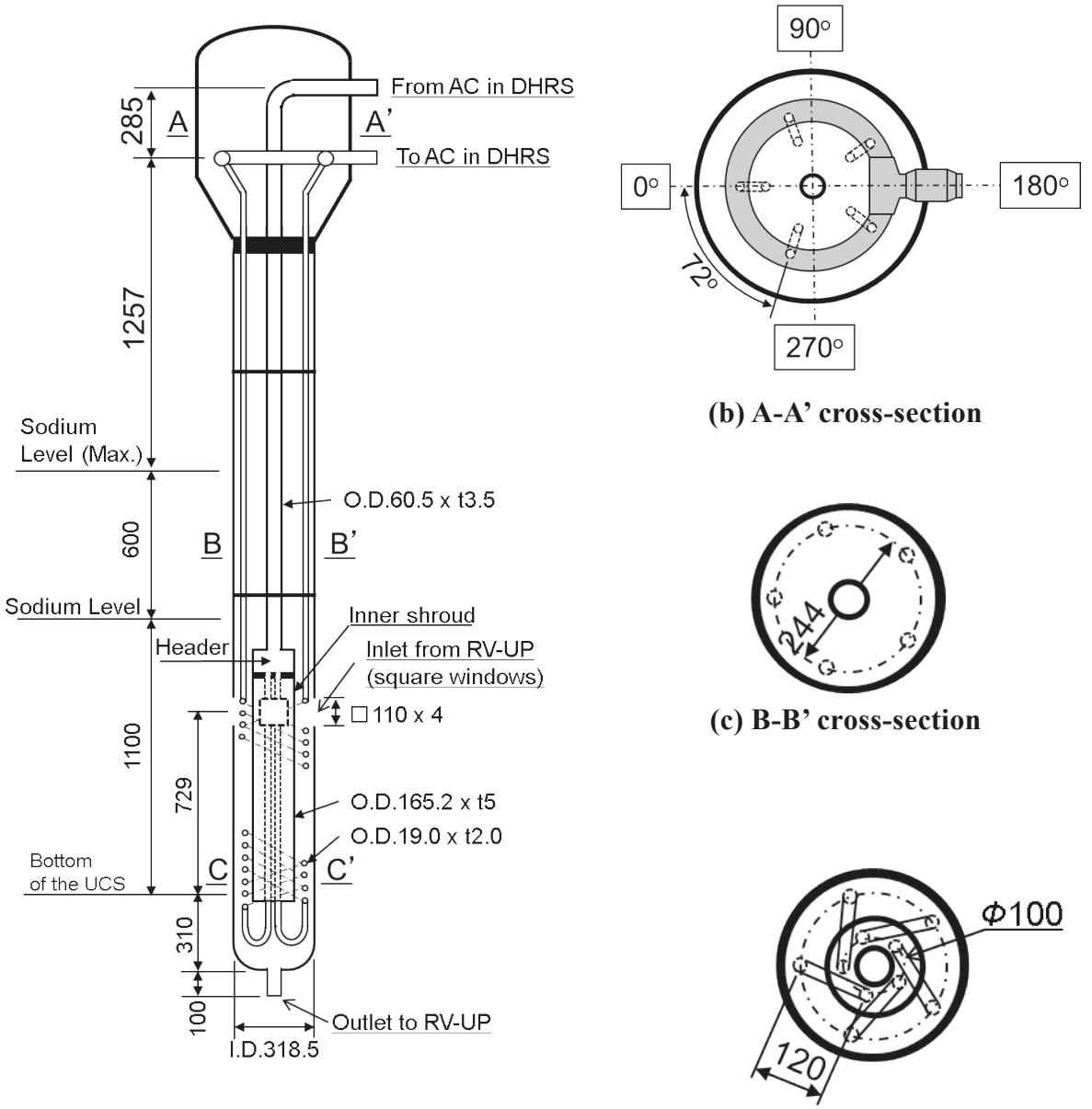


**(a) Vertical cross-section**

**(b) A-A' cross-section**

**(c) B-B' cross-section**

**(d) C-C' cross-section**

(Unit: mm)

**Figure 19 Dimensions of D-DHX in UP-RV.**

## 2.7 Other Components

### 2.7.1 Auxiliary Sodium Heater

To control the sodium temperature to set up the experimental conditions, an auxiliary sodium heater, comprising 76 electric heater pins with a capacity of 680 kW, was installed in the test loop. The auxiliary heater was only used to set the experimental condition before measurement. The loop to the auxiliary heater was closed by valves during the test. The auxiliary heater bypassing the simulated core is not within the scope of the present benchmark analysis.

### 2.7.2 Sodium Valves

Table 15 lists the specifications of the valves regarding the benchmark analysis in the apparatus with illustrations of the needle- and globe-type sodium valves used in the PLANDTL-DHX.

**Table 15 Specifications of major sodium valves (SVs) in the PHTS.**

| Location (see Fig. 15) | ID No. (Tag No.) | Valve type(*1) | Inner diameter, $D_0$ (m) | Lift length, $L_0$ (m) |
|---|---|---|---|---|
| PHTS | SV1 (SV101M) | Needle | 0.1063 | 0.05 |
| Outer assemblies (A-C) | SV3 (SV103M) | Needle | 0.1063 | 0.03 |
| Outer assemblies (D-F) | SV4 (SV104M) | Needle | 0.1063 | 0.03 |
| Center assembly | SV5 (SV105M) | Globe | 0.0535 | 0.018 |
| Center assembly | SV5a (SV105A) | Globe | 0.0535 | (0.018) |

(*1) Illustrations of typical sodium valves

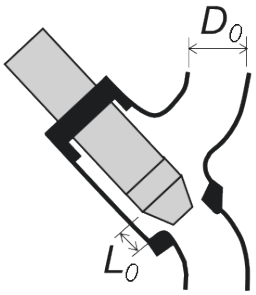


**(a) Needle valve**

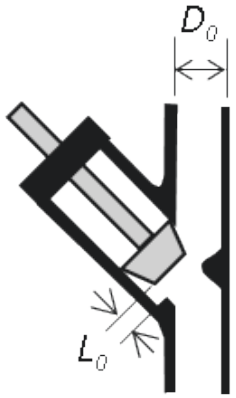


**(b) Globe valve**

## 2.8 Measurement System

### 2.8.1 Data Recording System

The measured data, including temperature, flowrate, differential pressure, and heater output, were recorded to the hard disk storage of a computer (HP A900) in the recording system, which could record a total of 880 signals of the measured data at an interval of $16\times10^{-3}$ s. The measured data from sensors were converted to physical quantities using the data conversion equations derived from the results of the calibration of thermocouples, flowmeters, and differential pressure sensors.

### 2.8.2 Temperature Measurement

The thermocouple output signals were recorded after they passed through a zero-junction compensator, a direct-current amplifier (gain: 200 times), and a 13-bit analog-to-digital converter.

In the calibration, relative calibration of thermocouples was performed before and after the tests in each campaign. To establish an isothermal state at several calibration temperatures in the RV, the operation was performed at the maximum flowrates in the PHTS, SHTS, DHRS, and the gap region of the core. The flowrate through the core was maintained at $1.667\times10^{-3}$ $m^3/s$ (100 liter/min) to control the RV outlet temperature at the calibration target temperature using the auxiliary sodium heater (see Subsection 2.7.1). This condition was maintained for a minimum of 1800 s to achieve an isothermal state in the RV. Under this condition, data from all thermocouples installed in the RV as well as those in HTS (PHTS and SHTS) were recorded for 60 s at a sampling time of $16\times10^{-3}$ s. Thus, the relative calibration of each thermocouple was performed using the time-averaged data obtained from the reference temperatures measured by the thermocouple on the AE cross-section (0.116 m below the lower end of the heated section as shown in Fig. 22) in the center assembly. Electric heaters for preheating the apparatus were switched off during the calibration. Calibration data was obtained at 300 °C, 400 °C, and 500 °C while increasing the heater power and at 450 °C and 350 °C while decreasing the power to check the hysteresis of the thermocouples.

### 2.8.3 Flowrate Measurement

To measure the flowrate by EMFs (see Figs. 2 & 15 for their locations), direct calibration was performed using the volumetric calibration method. Before testing, all EMF data were recorded under a zero-flowrate state that was achieved by closing all valves. The calibration of the flowmeter was conducted in two steps. In the first step, direct calibration using the volumetric calibration method was performed as follows: A certain volume of sodium stocked in the expansion tank at the highest location of the PHTS was sent down to the sodium storage tank in the basement room through EMF1 (EMF101) in the PHTS. The flowrate was controlled by the opening condition of the SV1 sodium valve. Thus, EMF1 was calibrated first. EMF-B (EMF102), which does not appear in any figures of this document, was located at the branch pipeline of the PHTS in parallel to the main piping of EMF101 for use in measurement under low flowrate conditions. EMF-B was also calibrated directly by the volumetric calibration method in the same way as EMF101. Using EMF-B, which can measure low flowrate driven by the pony-EMP (EMP102) (this does not appear in any figures of this document) in the branch line, relative calibration was performed for EMF3, EMF4, and EMF5 for the flowrate to the simulated core. In DHRS, EMF6 was calibrated by the volumetric calibration method using the expansion tank located at the top of the DHRS. Table 16 lists the measurement range of EMFs (EMF1, EMF3, EMF4, and EMF5)

for the test section.

### 2.8.4 Pressure Difference Measurement

Pressure sensors were installed to measure the pressure difference between the upstream and downstream sides of the primary pump, pony pump, and the pump of DHRS. One line from the upstream side for lower pressure and another line from the downstream side for high pressure were connected to the argon gas supply system, which was equipped with closing valves and a digital manometer to measure the reference pressure. In the calibration, both lower- and higher-pressure lines were opened to the atmosphere to adjust the output to zero for the reference pressure. During the calibration, the valve in the lower-pressure line was opened to set at 0 Pa at all times. The pressure on the high-pressure line was adjusted at the calibration pressure by the argon gas. The output of the pressure difference sensor was recorded after the pressure reached the calibration value, the valve in the high-pressure line was closed, and the stable state was maintained for 600 s.

**Table 16 Measurement range of EMFs for the test section.**

| Location (see Fig. 2) | ID No. | Unit | Measurement range |
|---|---|---|---|
| PHTS between IHX and LP | EMF1 | $10^{-3}$ $m^3/s$ | -5 ～ 20 |
| Inlet of the center assembly | EMF5 | | -2.5 ～ 5.833 |
| Inlet of outer assemblies, A to C | EMF3 | | -5 ～ 10 |
| Inlet of outer assemblies, D to F | EMF4 | | -5 ～ 10 |

**3. Selectable Models for Benchmark Analyses**

As listed in Table 17, the simulation model for the benchmark analysis is selectable depending on the objective of the participants. Participants whose target area includes the RV only to perform analysis focused on the RV can select, for instance, from three approaches to modeling and simulation: a multi-dimensional computational fluid dynamics (CFD) model for the RV, a one-dimensional plant dynamics (1D) model with a flow network approach and coupling of the CFD model for UP-RV and a 1D model for the core. Another participant whose target area includes both the RV and PHTS to perform analysis focused on the PHTS can select, for instance, from three approaches: a fully 1D model for both the RV and PHTS, a fully CFD model for both, and a coupling of a CFD model for the RV and a 1D model for the PHTS. In the latter option with the PTHS modeling, pressure drop between up- and down-stream of the EMP101 (see Fig. 35) may be used for boundary condition, instead of the direct use of the flow-rate measurements (see. Figs. 32(b) and (c)).

In the benchmark analyses, the reference model is a coupled analysis with the CFD model for the RV including the core and 1D model for the PHTS with boundary conditions at the IHX inlet in the SHTS and the D-DHX inlet for Case-DRACS or the PHX inlet for Case-PRACS.

**Table 17 Selectable analysis models for benchmark analyses.**

<table>
<tr><th rowspan="2">Target domain</th><th rowspan="2">Selectable model (for instance)</th><th colspan="4">Boundary conditions</th><th rowspan="2">Geometry data</th></tr>
<tr><th>Flowrate</th><th>Temperature</th><th>Power</th><th>Pressure Difference</th></tr>
<tr><td rowspan="3">RV only</td><td>One-dimensional plant dynamics (1D) model</td><td rowspan="3">F3, F4, and F5 at the inlets of the center, outer A-C, and outer E-F assemblies as in Fig. 32</td><td rowspan="3">T3, T4, and T5 at the inlets of the center, outer A-C, and outer E-F assemblies as in Fig. 33</td><td rowspan="5">Q1, Q2, and Q3 as in Fig. 34</td><td>-</td><td rowspan="3">Subsections of 2.2 for the RV and 2.6 for the DHRS</td></tr>
<tr><td>Multi-dimensional CFD (CFD) model</td><td></td></tr>
<tr><td>1D model for the core and CFD model for the UP-RV</td><td></td></tr>
<tr><td rowspan="3">RV and PHTS including IHX</td><td>Full 1D model</td><td rowspan="3">F2 at the IHX inlet in the SHTS as in Fig. 32 (a-1) and Fig. 32 (a-2)</td><td rowspan="3">T2 at the IHX inlet in the SHTS as in Fig. 33 (b-1) and Fig. 33 (b-2)</td><td rowspan="3">PD1 for a pressure difference among the EMP101 as in Fig. 35</td><td rowspan="3">Subsections of 2.2 for the RV, 2.3 for the PHTS, 2.4 for the IHX, and 2.6 for the DHRS</td></tr>
<tr><td>Full CFD model</td></tr>
<tr><td>A coupling of 1D model for the PHTS and CFD model for the RV (reference)</td></tr>
</table>

## 4. Locations of Measured Data for Benchmark Analysis

Figure 20 and Table 18 show the locations of the sensors whose measurements are utilized to define the boundary conditions in HTSs in the PLANDTL-DHX.

### 4.1 Flowrates

Table 19 lists the points for comparison in HTSs to be utilized in the benchmark analyses.

In case of analysis focused on the RV, the flowrates measured at Inlet-A by EMF3 (EMF105) for the center assembly, indexed as F3, Inlet-B by EMF4 (EMF103) for the outer assemblies of A, B, and C, indexed as F4, and Inlet-C by EMF5 (EMF104) for the outer assemblies of D, E, and F, indexed as F5, represent the boundary conditions at the RV inlets.

For analysis focused on the PHTS, the flowrate through DRACS or PRACS was measured by EMF6 (EMF801), indexed as F6, and the flowrate at the IHX inlet on the SHTS side was measured by EMF2 (EMF201), indexed as F2, represent the boundary conditions. The flowrates of F3, F4, and F5 are to be compared with the numerical results. Flowrate through the PHTS is estimated as the summation of flowrates, F3, F4, and F5. The flowrate measured by EMF1 (EMF101), indexed as F1, is shown just for information.

### 4.2 Temperatures

Tables 19 and 20 list, respectively, the points for comparison in HTSs and in the core to be utilized in the benchmark analyses. Representative thermocouples in the pin bundle on the axial and horizontal cross-sections are selected for comparison with the numerical results.

#### 4.2.1 Temperatures in UP-RV

Figure 21 shows the axial positions of thermocouples installed in thermo-couple (TC)-tree 2 as an example. The temperature distributions in the UP-RV were measured by TC-tree 2, TC-2, at 30$^{o}$, TC-3 at 150$^{o}$, and TC-1 at 315$^{o}$. Temperature data measured by these thermocouples were selected for the benchmark analyses. Tables 21, 22, and 23 list, respectively, the locations of the thermocouples installed in TC-2, TC-3, and TC-1.

#### 4.2.2 Temperatures in Simulated Core

Table 24 lists the indexes and locations of thermocouples on Line-C0, Line-C1, and Line-C2, respectively, at the core center and two peripheral locations in the center assembly. As for the axial temperature profiles, Line-C0 around the center pin of the center assembly, Line-C1 and Line-C2 around the outer positions of the center assembly to pair with Line-G1 and Line-G2 in the inner IWGs, respectively, were selected to compare the temperature distribution in the benchmark analyses. Line-G3 and Line-G4 are located in the outer IWGs. Table 25 lists the indexes and locations of thermocouples on Line-G4, Line-G2, Line-G1, and Line-G3 in the IWGs. Thermocouples on Line-C1 and Line-C2 are paired with those on Line-G1 and Line-G2 to evaluate the RHT through the wrapper tube of the center assembly.

Figure 22 shows the locations of vertical cross-sections on which thermocouples were installed. Thermocouples were installed in the assemblies on horizontal cross-sections, AE, BA, BD, BI, CB and

DC. In Figures 23 to 28, the locations of thermocouples are shown on the cross-sections of, respectively, AE, BA, BD, BI, CB, and DC. The horizontal profiles on cross-sections AE in the lower non-heated section, BA in the lower end of the heated section, BD in the middle of the heated section, BI in the upper end of the heated section, CB in the upper non-heated section, and DC in the neutron shield section were selected for comparison in the benchmark analyses. Tables 26 to 31 show the indexes and locations of thermocouples on, respectively, cross-sections, AE, BA, BD, BI, CB, and DC.

### 4.2.3 Temperatures in PHTS

Temperatures measured at the RV outlet by TIC112 (TPN171), indexed as T8, the IHX inlet by TI113 (TPN174) in the hot-leg piping of the PHTS, and the IHX outlet in the cold-leg piping of the PHTS by TIC114 (TPN181) are to be compared with the numerical results. Temperatures measured at the LP by TI101 (TPW115), indexed as T1, the Inlet-A for the center assembly by TIA106 (TPW151), indexed as T5, the Inlet-B for outer assemblies of A, B, and C by TIA104 (TPW131), indexed as T3, and Inlet-C for outer assemblies of D, E, and F by TIA105 (TPW141), indexed as T4 are to be compared with the numerical results, and they are to be used as the boundary conditions in case of an analysis focused on the RV.

### 4.2.4 Temperatures in SHTS

Temperature measured at the IHX inlet in the SHTS by TI201 (TPN201), indexed as T2, is to be used for the boundary condition. On the other hand, the temperature measured at the IHX outlet in the SHTS by TI202 (TPN202), indexed as T11, was selected for comparison with the numerical result to check the heat transfer model between the PHTS and the SHTS in the IHX.

### 4.2.5 Temperatures in DHRS

In the DHRS, the temperature measured at the D-DHX inlet by TI801 (TPN804), indexed as T6, is to be used for the boundary condition in Case-DRACS, and the temperature measured at PHX Inlet by TR807 (TPN813), indexed as T7, is to be used for the boundary condition in Case-PRACS. The temperature measured at the D-DHX Outlet by TI802 (TPN805), indexed as T12, and the temperature measured at PHX Outlet by TPN814, indexed as T13, were selected for comparison with the numerical results to check the heat transfer model between UP-RV and DHRS in the D-DHX or PHX, respectively.

Figures 29 (a), (b), and (c) show the locations of thermocouples in the D-DHX. In the D-DHX, temperatures measured at the D-DHX inlets indexed as D1 and D2, and those at the D-DHX outlet, indexed as D3 and D4, were selected for comparison with the numerical results.

**Table 18 Locations of sensors for boundary conditions.**
**(see Fig. 30)**

| HTS | Physical quantity | Locations | Tag No. | Index (Fig. 20) |
|---|---|---|---|---|
| PHTS | Flowrate | RV inlet (Outer A-C) | EMF3 (EMF103) | F3 |
| | | RV inlet (Outer D-F) | EMF4 (EMF104) | F4 |
| | | RV inlet (Center) | EMF5 (EMF105) | F5 |
| | | PHTS | EMF1 (EMF101) | F1 |
| | Pressure Difference | EMP-PHTS | PD1 (PD104) | PD1 |
| | Temperature (Inlet) | LP | TI101 (TPW115) | T1 |
| | | RV inlet (Outer A-C) | TIA104 (TPW131) | T3 |
| | | RV inlet (Outer D-F) | TIA105 (TPW141) | T4 |
| | | RV inlet (Center) | TIA106 (TPW151) | T5 |
| | Heater Power | Center assembly | Power 1-3 | Q1 |
| | | Outer 3 assemblies of A-C | Power 4-6 | Q2 |
| | | Outer 3 assemblies of D-F | Power 7-9 | Q3 |
| SHTS | Flowrate | IHX inlet | EMF2 (EMF201) | F2 |
| | Temperature (Inlet) | IHX inlet | TI201 (TPN201) | T2 |
| DRACS /PRACS | Flowrate | D-DHX/PHX inlet | EMF6 (EMF801) | F6 |
| | Temperature (Inlet) | D-DHX inlet | TI801 (TPN804) | T6 |
| | | PHX inlet | TR807 (TPN813) | T7 |

**Table 19 Comparison points in HTSs for benchmark analyses.**

| HTS | Physical quantity | Locations | Tag No. | Index (*) |
|---|---|---|---|---|
| PHTS | Flowrate | RV inlet (Center) | EMF5 (EMF105) | F5 (B.C.) |
| | | RV inlet (Outer A-C) | EMF3 (EMF103) | F3 (B.C.) |
| | | RV inlet (Outer D-F) | EMF4 (EMF104) | F4 (B.C.) |
| | | Primary flowrate | F3+F4+F5 | F0 (B.C.) |
| | | (Supportive data) | EMF1 (EMF101) | F1 |
| | Pressure Difference | EMP-PHTS | PD1 (PD104) | PD1 (B.C.) |
| | Temperature | RV outlet (Hot-leg temperature) | TIC112 (TPN171) | T8 |
| | | IHX inlet (Hot-leg temperature) | TI113 (TPN174) | - |
| | | IHX outlet (Cold-leg temperature) | TIC114 (TPN181) | - |
| | | LP (Cold-leg temperature) | TI101 (TPW115) | T1 (B.C.) |
| | | RV inlet (Center) | TIA106 (TPW151) | T5 (B.C.) |
| | | RV inlet (Outer A-C) | TIA104 (TPW131) | T3 (B.C.) |
| | | RV inlet (Outer D-F) | TIA105 (TPW141) | T4 (B.C.) |
| UP-RV | Temperature | TC-tree 1 at 30 degrees (see Fig. 4) | (Table 23) | TC-1 |
| | | TC-tree 2 at 150 degrees (see Fig. 4) | (Table 21) | TC-2 |
| | | TC-tree 3 at 315 degrees (see Fig. 4) | (Table 22) | TC-3 |
| | | DHX inlet | (Fig. 29) | D1 |
| | | DHX inlet | (Fig. 29) | D2 |
| | | DHX outlet | (Fig. 29) | D3 |
| | | DHX outlet | (Fig. 29) | D4 |
| SHTS | Flowrate | SHTS flowrate (at IHX inlet) | EMF2 (EMF201) | F2 (B.C) |
| | Temperature | IHX inlet | TI201 (TPN201) | T2 (B.C) |
| | | IHX outlet | TI202 (TPN202) | T11 |
| DRACS /PRACS | Flowrate | DRACS flowrate | EMF6 (EMF801) | F6 (B.C) |
| | Temperature | DHX inlet | TI801 (TPN804) | T6 (B.C) |
| | | DHX outlet | TI802 (TPN805) | T12 |
| | | PHX inlet | TR807 (TPN813) | T7 (B.C) |
| | | PHX outlet | - (TPN814) | T13 |

(*) The designation “B.C” indicates a boundary condition.

**Table 20 Comparison points of temperatures in the core for benchmark analyses.**

| Traverse line | Location(*1) | Region | Typical position (m) | TC Location |
|---|---|---|---|---|
| Axial profile | Line-C0 | Center assembly | (center pin No.101) | Table 24 |
| | Line-C1 | Center assembly | (pin No.402 or 403) | |
| | Line-C2 | Center assembly | (pin No.411 or 412) | |
| | Line-G1 | Inner gap (right side) | $y$ = 39.0 | Table 25 |
| | Line-G2 | Inner gap (left side) | $y$ = -39.0 | |
| | Line-G3 | Outer gap (right side) | $y$ = 115.3 | |
| | Line-G4 | Outer gap (left side) | $y$ =-115.3 | |
| Horizontal profile (see Fig. 22) | AE | Lower non-heated section | z = -1.160 | Table 26 |
| | BA | Lower heated section | z = -0.995 | Table 27 |
| | BD | Middle heated section | z = -0.500 | Table 28 |
| | BI | Upper heated section | z = -0.005 | Table 29 |
| | CB | Upper non-heated section | z = 0.325 | Table 30 |
| | DC | Neutron shield section | z = 1.100 | Table 31 |

(*1) Locations of the TC for axial profiles

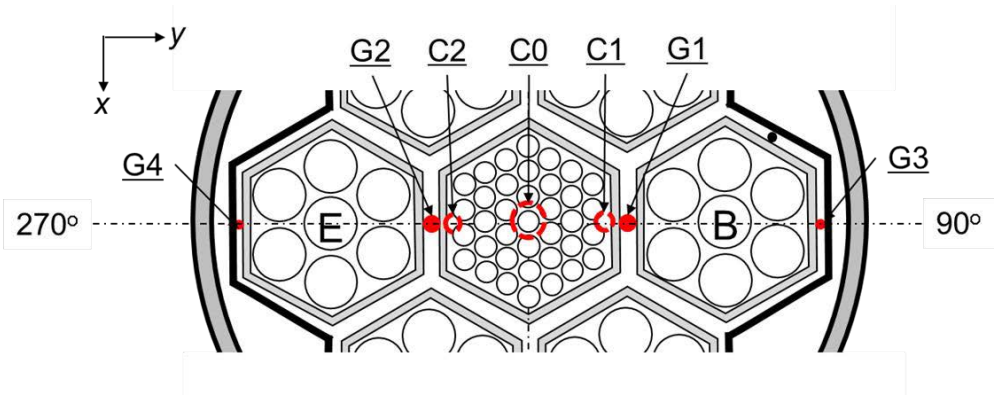

**Table 21 Locations of thermocouples on thermocouple-tree TC2 at 30 º in UP-RV. (see Fig. 4)**

| Index | TC tag No. | Location, z (m) | Location in Fig. 21 |
|---|---|---|---|
| TC2-1 | TRI030a-02 | 1.800 | U1 |
| TC2-2 | TRI030a-04 | 1.600 | U2 |
| TC2-3 | TRI030a-06 | 1.400 | U3 |
| TC2-4 | TRI030a-09 | 1.200 | U4 |
| TC2-5 | TRI030a-13 | 1.000 | U5 |
| TC2-6 | TRI030a-17 | 0.800 | U6 |
| TC2-7 | TRI030a-20 | 0.600 | U7 |
| TC2-8 | TRI030a-21 | 0.500 | U8 |
| TC2-9 | TRI030a-22 | 0.400 | U9 |
| TC2-10 | TRI030a-23 | 0.300 | U10 |
| TC2-11 | TRI030a-24 | 0.200 | U11 |
| TC2-12 | TRI030a-25 | 0.100 | U12 |
| TC2-13 | TRI030a-26 | 0.0 | U13 |
| TC2-14 | TRI030a-27 | -0.100 | U14 |
| TC2-15 | TRI030a-28 | -0.200 | U15 |
| TC2-16 | TRI030a-29 | -0.3 | U16 |

**Table 22 Locations of thermocouples on thermocouple-tree TC3 at 150 º in UP-RV. (see Fig. 4)**

| Index | TC tag No. | Location, z (m) | Location in Fig. 21 |
|---|---|---|---|
| TC3-1 | TRI150a-02 | 1.800 | U1 |
| TC3-2 | TRI150a-04 | 1.600 | U2 |
| TC3-3 | TRI150a-06 | 1.400 | U3 |
| TC3-4 | TRI150a-08 | 1.200 | U4 |
| TC3-5 | TRI150a-10 | 1.000 | U5 |
| TC3-6 | TRI150a-12 | 0.800 | U6 |
| TC3-7 | TRI150a-14 | 0.600 | U7 |
| TC3-8 | TRI150a-15 | 0.500 | U8 |
| TC3-9 | TRI150a-16 | 0.400 | U9 |
| TC3-10 | TRI150a-17 | 0.300 | U10 |
| TC3-11 | TRI150a-18 | 0.200 | U11 |
| TC3-12 | TRI150a-19 | 0.100 | U12 |
| TC3-13 | TRI150a-20 | 0.0 | U13 |
| TC3-14 | TRI150a-21 | -0.100 | U14 |
| TC3-15 | TRI150a-22 | -0.200 | U15 |
| TC3-16 | TRI150a-23 | -0.3 | U16 |

**Table 23 Locations of thermocouples on thermocouple-tree TC1 at 315 º in UP-RV. (see Fig. 4)**

| Index | TC tag No. | Location, z (m) | Location in Fig. 21 |
|---|---|---|---|
| TC1-1 | TRI315a-02 | 1.800 | U1 |
| TC1-2 | TRI315a-04 | 1.600 | U2 |
| TC1-3 | TRI315a-06 | 1.400 | U3 |
| TC1-4 | TRI315a-08 | 1.200 | U4 |
| TC1-5 | TRI315a-10 | 1.000 | U5 |
| TC1-6 | TRI315a-12 | 0.800 | U6 |
| TC1-7 | TRI315a-14 | 0.600 | U7 |
| TC1-8 | TRI315a-15 | 0.500 | U8 |
| TC1-9 | TRI315a-16 | 0.400 | U9 |
| TC1-10 | TRI315a-17 | 0.300 | U10 |
| TC1-11 | TRI315a-18 | 0.200 | U11 |
| TC1-12 | TRI315a-19 | 0.100 | U12 |
| TC1-13 | TRI315a-20 | 0.0 | U13 |
| TC1-14 | TRI315a-21 | -0.100 | U14 |
| TC1-15 | TRI315a-22 | -0.200 | U15 |
| TC1-16 | TRI315a-23 | -0.3 | U16 |

**Table 24 Locations of thermocouples at the core center (Line-C0) and peripheral gaps (Line-C1 and Line-C2) in the center assembly.**

| Traverse line | | Line-C0 (*1) | | |
|---|---|---|---|---|
| TC index | TC tag No. | x (mm) | y (mm) | z (mm) |
| AE1 | TBA101AE | -4.7 | 1.3 | -1160 |
| BA1 | TSA101BA | 4.4 | 0.0 | -995 |
| BC1 | TSA101BC | 4.4 | 0.0 | -665 |
| BD1 | TSA101BD | -3.1 | 3.1 | -500 |
| BE1 | TSA101BE | 4.4 | 0.0 | -335 |
| BG1 | TSA101BG | -3.1 | 3.1 | -170 |
| BI1 | TVA101BI | -3.5 | -3.5 | -5 |
| CB1 | TSA101CB | -3.1 | 3.1 | 325 |
| DA1 | TNS000DA | 0.0 | 0.0 | 600 |
| DB1 | TNS000DB | 0.0 | 0.0 | 850 |
| DC1 | TNS000DC | 0.0 | 0.0 | 1100 |
| Traverse line | | Line-C1 (*2) | | |
| TC index | TC tag No. | x (mm) | y (mm) | z (mm) |
| BA4 | TSA402BA | 28.8 | -1.8 | -995 |
| BC8 | TSA402BC | 28.8 | -1.8 | -665 |
| BD7 | TSA403BD | 28.8 | 1.8 | -500 |
| BE7 | TSA402BE | 28.8 | -1.8 | -335 |
| BG17 | TSA403BG | 28.8 | 1.8 | -170 |
| BI5 | TSA402BI | 28.8 | -1.8 | -5 |
| CB2 | TSA403CB | 28.8 | 1.8 | 325 |
| Traverse line | | Line-C2 (*3) | | |
| TC index | TC tag No. | x (mm) | y (mm) | z (mm) |
| BA5 | TSA412BA | -28.8 | -1.8 | -995 |
| BC9 | TSA412BC | -28.8 | -1.8 | -665 |
| BD8 | TWA411BD | -29.2 | 1.5 | -500 |
| BE8 | TSA412BE | -28.8 | -1.8 | -335 |
| BG20 | TWA411BG | -29.2 | 1.5 | -170 |
| BI6 | TWA411BI | -29.2 | 1.5 | -5 |
| CB3 | TSA412CB | -28.8 | -1.8 | 325 |

(*1) C0: TCs around the center pin No.101 in the center assembly (see Table 20)

(*2) C1: TCs around the pin No.402 or 403 in the right side peripheral subchannel of the center assembly (see Table 20)

(*3) C2: TCs around the pin No.411 or 412 in the left side peripheral subchannel of the center assembly (see Table 20)

**Table 25 Indexes and locations of thermocouples at the gaps.**

| Traverse line | Line-G4 (*1) | Line-G2 (*2) | Line-G1 (*3) | Line-G3 (*4) |
|---|---|---|---|---|
| Location, z (mm) | Location, $y$ (mm) at $x$ = 0 (mm) | | | |
| | -115.3 | -39.0 | 39.0 | 115.3 |
| -995 | BA26 | BA20 | BA14 | BA21 |
| -665 | BC7 | BC5 | BC4 | BC6 |
| -500 | BD32 | BD26 | BD20 | BD27 |
| -335 | BE6 | BE4 | ― | BE5 |
| -170 | BG16 | BG10 | BG4 | BG11 |
| -5 | BI30 | BI24 | BI18 | BI25 |
| 325 | CB18 | CB12 | CB6 | CB13 |
| 600 | DA11 | DA9 | DA4 | DA10 |
| 850 | DB15 | DB13 | DB8 | DB14 |
| 1100 | DC15 | DC13 | DC8 | DC14 |

(*1) G4: location at the left side gap on the outer assembly-E (see Table 20)

(*2) G2: location between the center assembly and the outer assembly-E (see Table 20)

(*3) G1: location between the center assembly and the outer assembly-B (see Table 20)

(*4) G4: location at the right side gap on the outer assembly-B (see Table 20)

**Table 26 Indexes and locations of thermocouples at AE cross-section. (Inlet non-heated position as in Fig. 23: at 1160 mm below the top of the heated section)**

| TC index | TC tag No. | Location | |
|---|---|---|---|
| | | $x$ (mm) | $y$ (mm) |
| AE1 | TBA101AE | -4.7 | 1.3 |
| AE2 | TBA101aAE | 31.1 | 59.7 |
| AE3 | TBA101bAE | 70.1 | -7.9 |
| AE4 | TBA101cAE | 31.1 | -75.4 |
| AE5 | TBA101dAE | -46.9 | -75.4 |
| AE6 | TBA101eAE | -85.9 | -7.9 |
| AE7 | TBA101fAE | -46.9 | 59.7 |

**Table 27 Indexes and locations of thermocouples at BA cross-section.**
**(Lower heated position as in Fig. 24: at 995 mm below the top of the heated section)**

| TC index | TC tag No. | Location | |
|---|---|---|---|
| | | *x* (mm) | *y* (mm) |
| BA1 | TSA101BA | 4.4 | 0.0 |
| BA2 | TSA302BA | 21.5 | 0.0 |
| BA3 | TSA308BA | -21.5 | 0.0 |
| BA4 | TSA402BA | 28.8 | -1.8 |
| BA5 | TSA412BA | -28.8 | -1.8 |
| BA6 | TSA101bBA1 | 85.5 | -7.5 |
| BA7 | TSA201bBA | 104.9 | -3.7 |
| BA8 | TSA204bBA | 53.3 | 2.0 |
| BA9 | TSA205bBA | 66.1 | -3.7 |
| BA10 | TSA101eBA1 | -70.5 | -7.5 |
| BA11 | TSA202eBA | -51.1 | 3.7 |
| BA12 | TSA204eBA | -89.9 | 3.7 |
| BA13 | TSA205eBA | -104.9 | -3.7 |
| BA14 | TGN090BA | 39.0 | 0.0 |
| BA20 | TGN207BA | -39.0 | 0.0 |
| BA21 | TGN090bBA | 115.3 | 0.0 |
| BA26 | TGN270eBA | -115.3 | 0.0 |

**Table 28 Indexes and locations of thermocouples at BD cross-section.**
**(Middle heated position as in Fig. 25: at 500 mm below the top of the heated section)**

| TC index | TC tag No. | Location | |
|---|---|---|---|
| | | *x* (mm) | *y* (mm) |
| BD1 | TSA101BD | -3.1 | 3.1 |
| BD2 | TSA201BD | 5.5 | -1.8 |
| BD3 | TSA205BD | -11.7 | -1.8 |
| BD4 | TSA302BD | 14.0 | 3.1 |
| BD5 | TSA308BD | -21.5 | 0.0 |
| BD6 | TSA402BD | 22.6 | -1.8 |
| BD7 | TSA403BD | 28.8 | 1.8 |
| BD8 | TWA411BD | -29.2 | 1.5 |
| BD9 | TSA101bBD1 | 70.5 | -7.5 |
| BD10 | TSA101bBD2 | 85.5 | -7.5 |
| BD11 | TSA201bBD | 104.9 | -3.7 |
| BD12 | TSA202bBD | 89.9 | 3.7 |
| BD13 | TSA204bBD | 51.1 | 3.7 |
| BD14 | TSA205bBD | 66.1 | -3.7 |
| BD15 | TSA101eBD1 | -85.5 | -7.5 |
| BD16 | TSA101eBD2 | -70.5 | -7.5 |
| BD17 | TSA201eBD | -66.1 | -3.7 |
| BD18 | TSA202eBD | -51.1 | 3.7 |
| BD19 | TSA205eBD | -104.9 | -3.7 |
| BD20 | TGN090BD | 39.0 | 0.0 |
| BD26 | TGN270BD | -39.0 | 0.0 |
| BD27 | TGN090bBD | 115.3 | 0.0 |
| BD32 | TGN270eBD | -115.3 | 0.0 |

**Table 29 Indexes and locations of thermocouples at BI cross-section.**
**(Top heated position as in Fig. 26: at 5 mm below the top of the heated section)**

| TC index | TC tag No. | Location | |
|---|---|---|---|
| | | *x* (mm) | *y* (mm) |
| BI1 | TVA101BI | -3.5 | -3.5 |
| BI2 | TVA202BI | 5.1 | 1.5 |
| BI3 | TVA204BI | -12.0 | 1.5 |
| BI4 | TVA304BI | 13.7 | -3.5 |
| BI5 | TSA402BI | 28.8 | -1.8 |
| BI6 | TWA411BI | -29.2 | 1.5 |
| BI7 | TSA101bBI2 | 85.5 | -7.5 |
| BI8 | TSA101bBI1 | 70.5 | -7.5 |
| BI9 | TSA201bBI | 104.9 | -3.7 |
| BI10 | TSA202bBI | 89.9 | 3.7 |
| BI11 | TSA204bBI | 51.1 | 3.7 |
| BI12 | TSA205bBI | 66.1 | -3.7 |
| BI13 | TSA101eBI2 | -70.5 | -7.5 |
| BI14 | TSA101eBI1 | -85.5 | -7.5 |
| BI15 | TSA201eBI | -66.1 | -3.7 |
| BI16 | TSA202eBI | -51.1 | 3.7 |
| BI17 | TSA204eBI | -89.9 | 3.7 |
| BI18 | TGN090BI | 39.0 | 0.0 |
| BI24 | TGN270BI | -39.0 | 0.0 |
| BI25 | TGN090bBI | 115.3 | 0.0 |
| BI30 | TGN270eBI | -115.3 | 0.0 |

**Table 30 Indexes and locations of thermocouples at CB cross-section.**
**(Upper non-heated position as in Fig. 27: at 325mm upper the top of heated section)**

| TC index | TC tag No. | Location (x, y) | |
|---|---|---|---|
| | | x (mm) | y (mm) |
| CB1 | TSA101CB | -3.1 | 3.1 |
| CB2 | TSA403CB | 28.8 | 1.8 |
| CB3 | TSA412CB | -28.8 | -1.8 |
| CB4 | TSA101bCB2 | 85.5 | -7.5 |
| CB5 | TSA101eCB2 | -70.5 | -7.5 |
| CB6 | TGN090CB | 39.0 | 0.0 |
| CB12 | TGN270CB | -39.0 | 0.0 |
| CB13 | TGN090bCB | 115.3 | 0.0 |
| CB18 | TGN270eCB | -115.3 | 0.0 |

**Table 31 Indexes and locations of thermocouples at DC cross-section.**
**(Outlet non-heated position as in Fig. 28: at 1100 upper the top of the heated section)**

| TC index | TC tag No. | Location | |
|---|---|---|---|
| | | *x* (mm) | *y* (mm) |
| DC1 | TNS000DC | 0.0 | 0.0 |
| DC2 | TNS000bDC | 78.0 | 0.0 |
| DC3 | TNS000eDC | -78.0 | 0.0 |
| DC8 | TGN090DC | 39.0 | 0.0 |
| DC13 | TGN270DC | -39.0 | 0.0 |
| DC14 | TGN090bDC | 115.3 | 0.0 |
| DC15 | TGN270eDC | -115.3 | 0.0 |

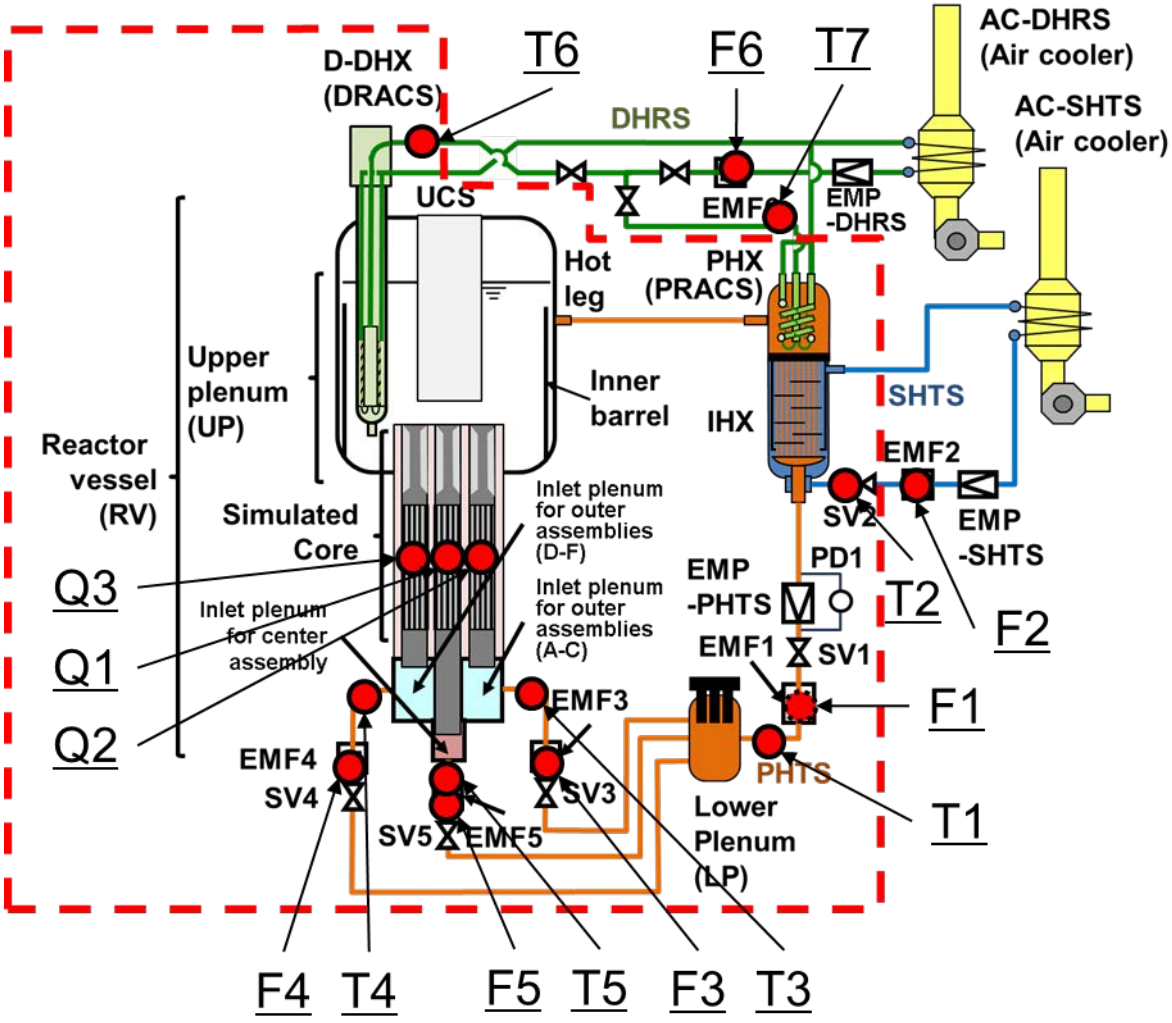


**Figure 20 Locations of sensors for boundary conditions.**
**(The area surrounded by the dotted red line corresponds to the area for benchmark analysis)**

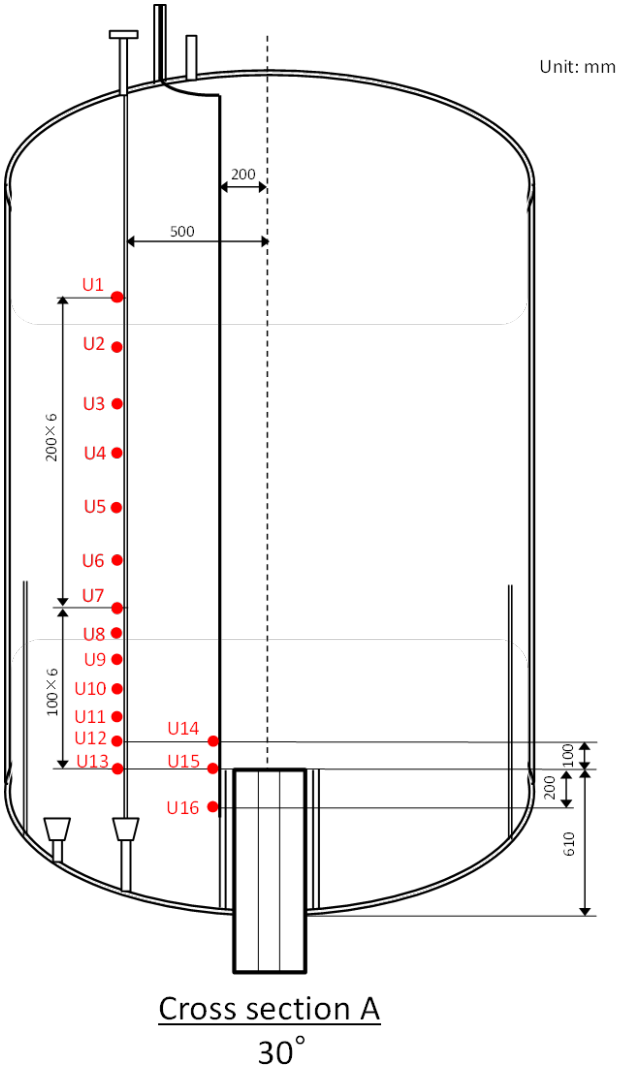


**Figure 21 Thermocouple locations on a TC tree installed in UP (TC-2 as an example).**

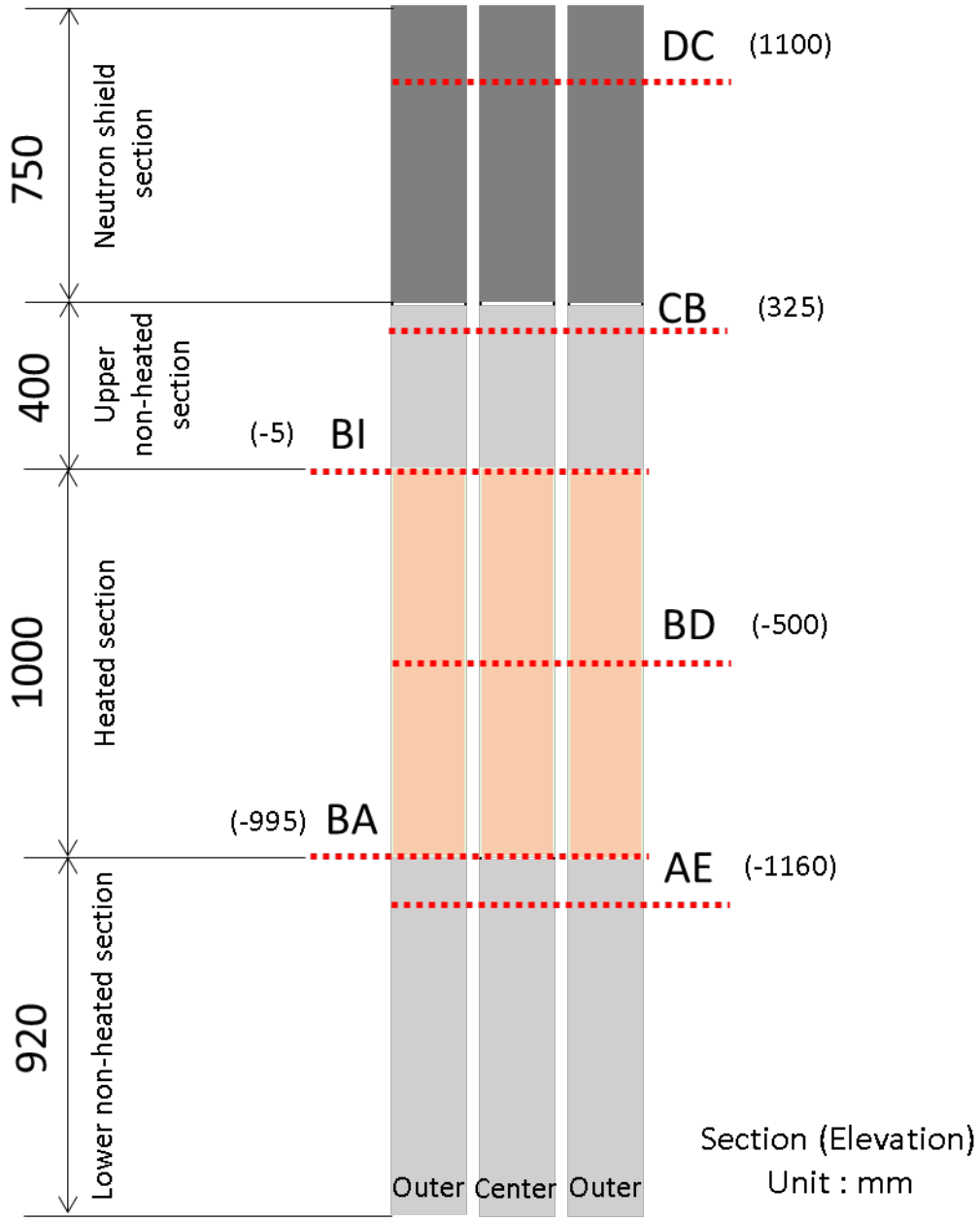


**Figure 22 Locations of vertical cross-sections on which thermocouples were installed.**

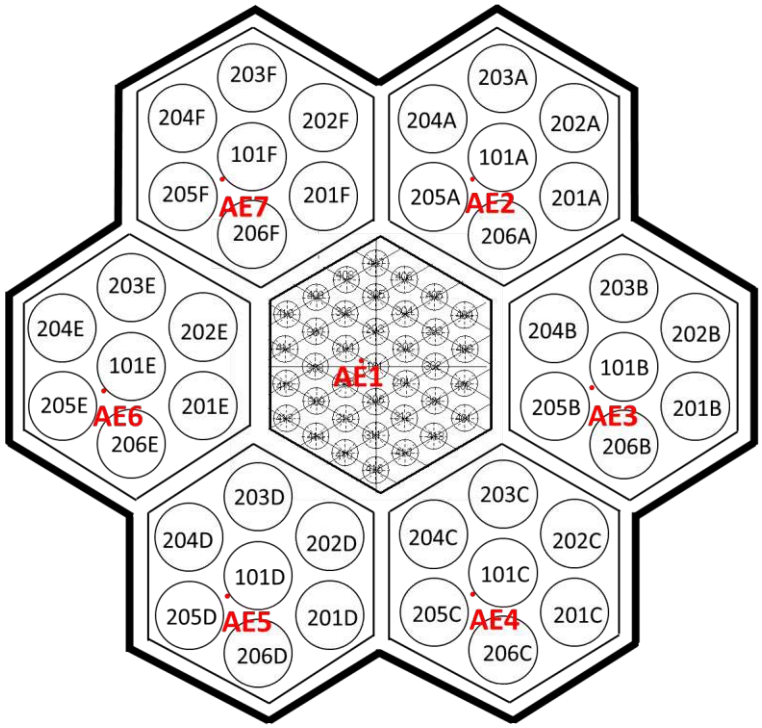


**Figure 23 Thermocouple locations on AE cross-section.**

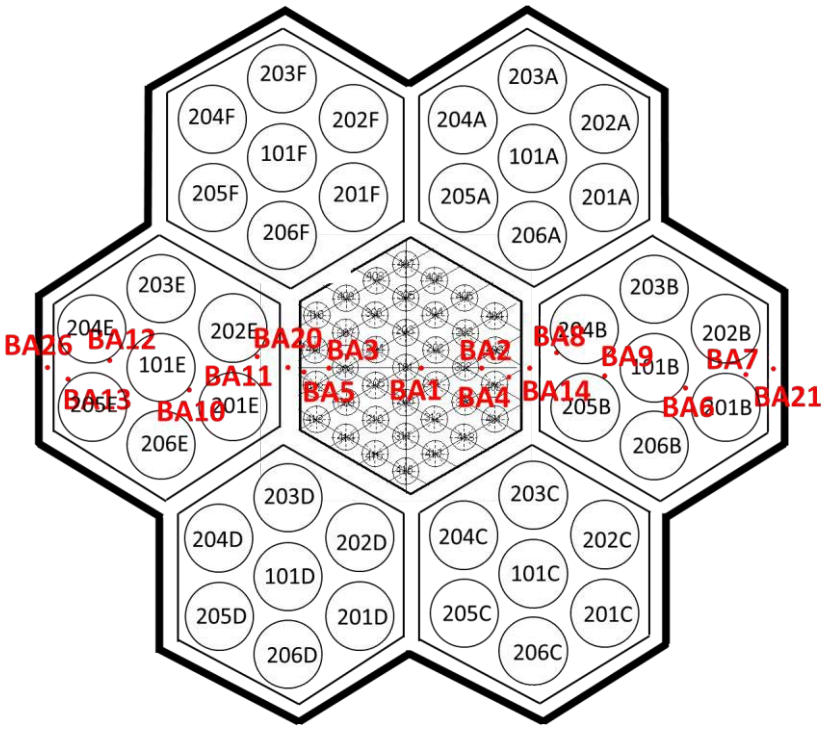


**Figure 24 Thermocouple locations on BA cross-section.**

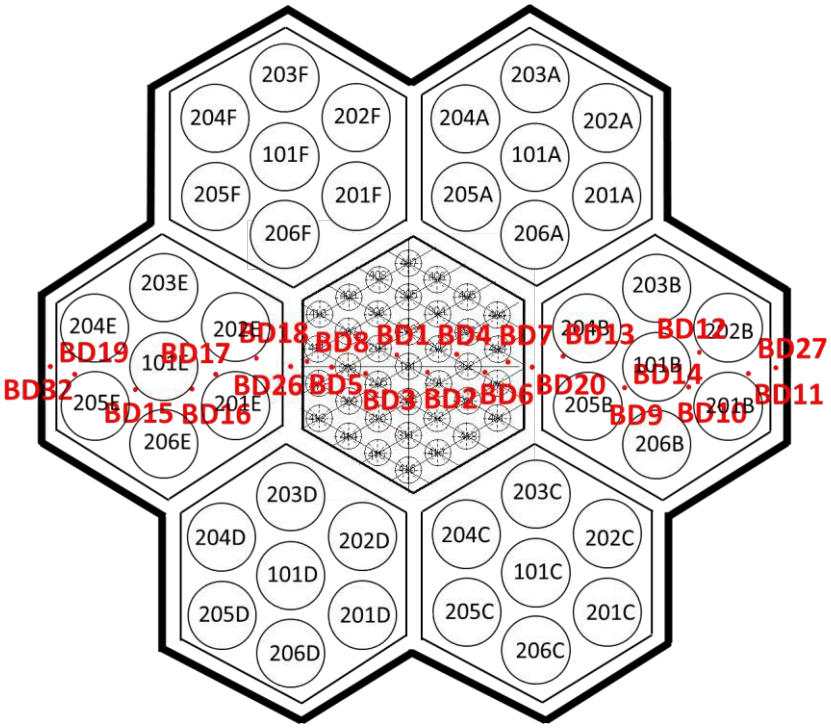


**Figure 25 Thermocouple locations on BD cross-section.**

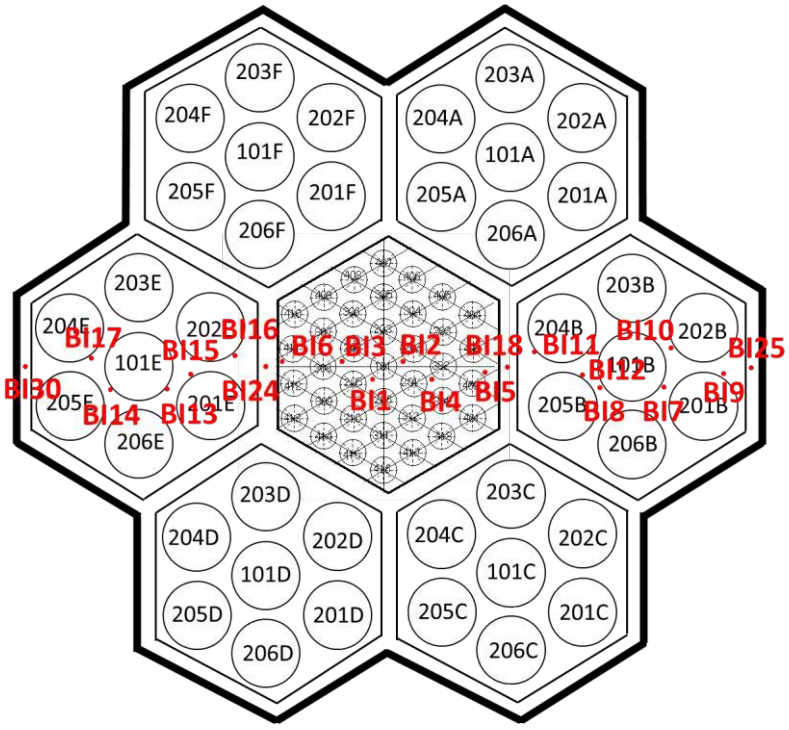


**Figure 26 Thermocouple locations on BI cross-section.**

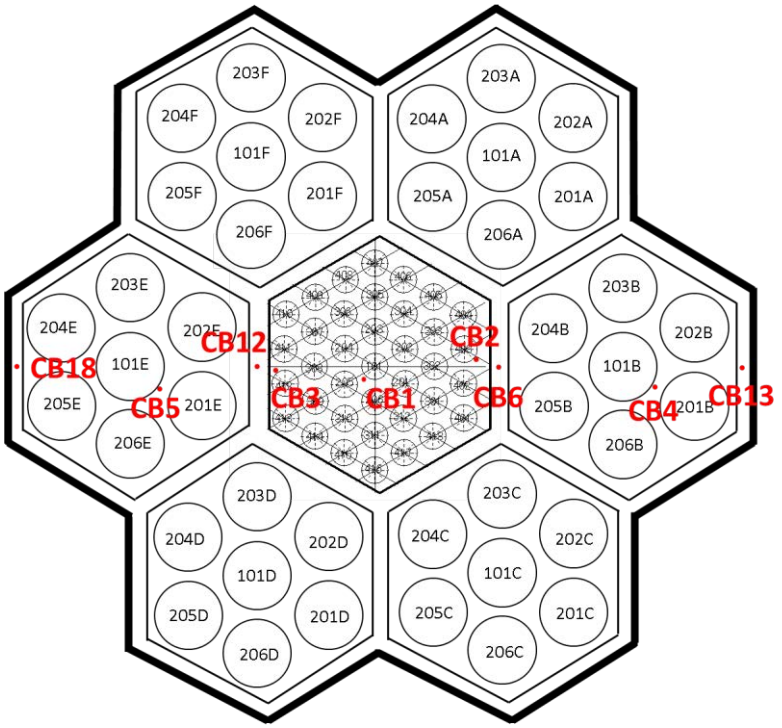


**Figure 27 Thermocouple locations on CB cross-section.**

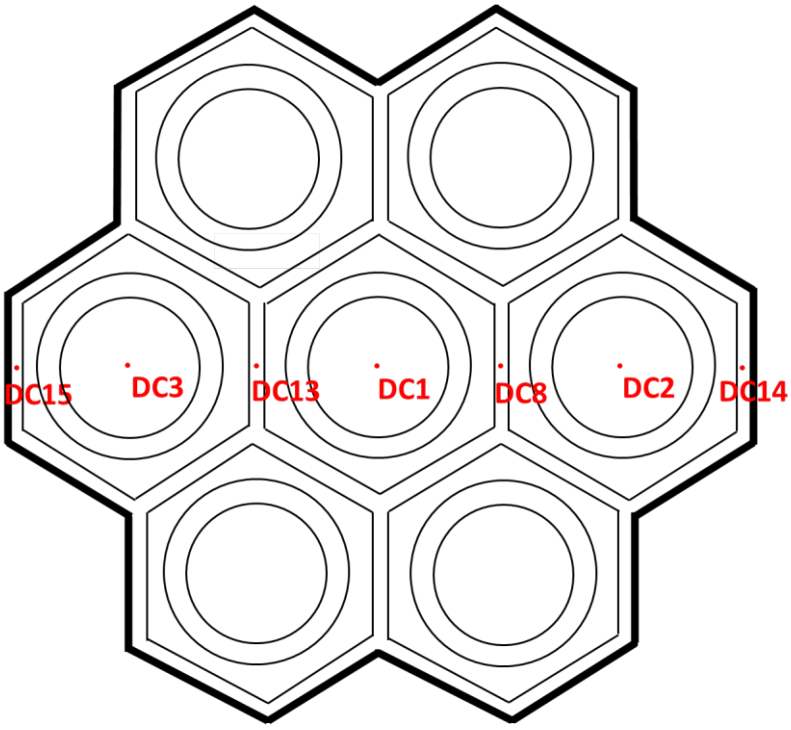


**Figure 28 Thermocouple locations on DC cross-section.**

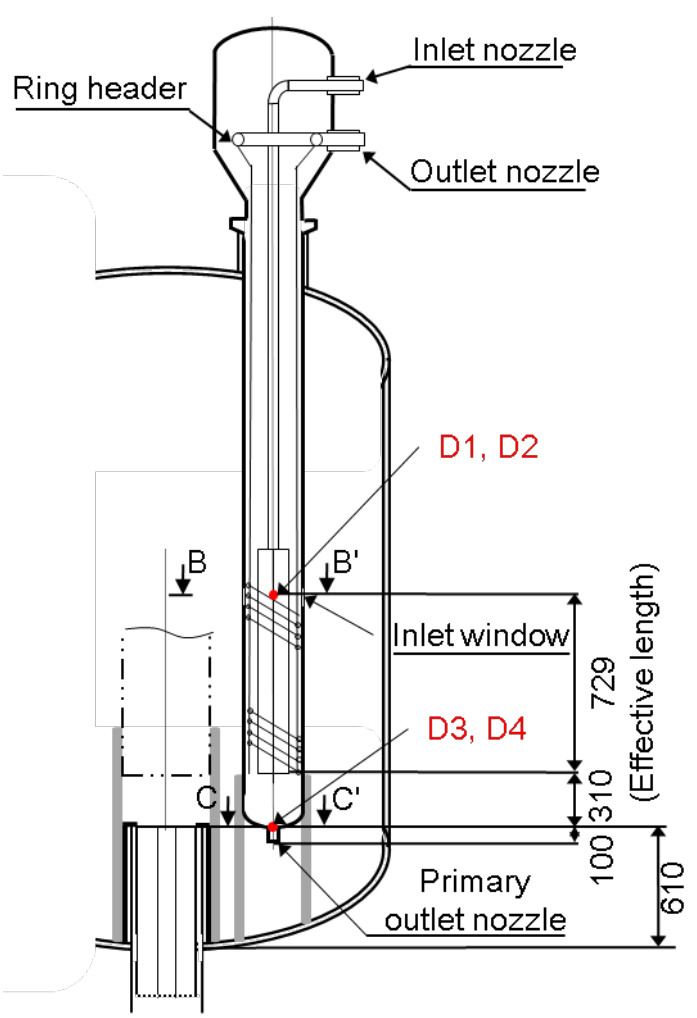


(a) Overview of D-DHX

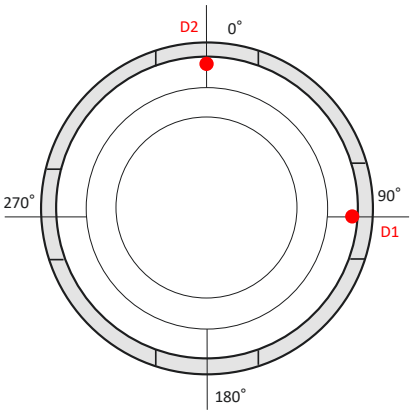


(b) Inlet windows of D-DHX
(Cross section B-B')

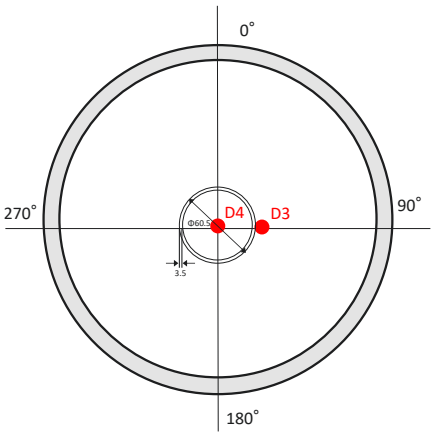


(c) Outlet nozzle of D-DHX
(Cross section C-C')

(Unit: mm)

**Figure 29 Locations of thermocouples in D-DHX.**

## 5. Boundary Conditions for Benchmark Analyses

### 5.1 Common Settings

During NC in the DHRS operation, the operating conditions of the DRACS or PRACS and the SHTS may influence the NC in the PHTS. To understand the effects of the operating conditions of these HTSs on the thermal-hydraulic phenomena in the core, system transient tests for an extended period of approximately 7,000 s from a scram event (SCRAM) were conducted using the PLANDTL-DHX. The test conditions simulated the plant transient behavior from a normal operating condition to an NC condition in the PHTS assuming a large-scale SFR with an electric power output of 1 GW. Figure 30 shows the performance specification on the valve flow coefficient (Cv) for the opening rate of SV1 (SV101M). Cv of SV1 has linearity to the valve opening rate from zero to Cv = 254 at the maximum.

### 5.2 Initial State

Table 32 lists the steady-state conditions: the time average and the standard deviation (in round brackets) for 28 s before the SCRAM at each test case.

In the PHTS, the flowrate was set at 12% ($5.7\times10^{-3}$ $m^3/s$) of the normal operating condition of the large-scale SFR (NOC), and the heater power was set to maintain the temperature set at the RV outlet (temperature data will be opened in the open-benchmark phase). It was difficult to reproduce the heater power and flowrate for the normal operating conditions at full power of the SFR due to the limited capacity of PLANDTL-DHX. In the SHTS, the blower of the AC-SHTS and the EMP-SHTS were operated to remove the heat generated at the simulated core to the atmosphere. The dumper of the AC-SHTS was closed. In the DHRS, the dumper of the AC-DHRS was closed without blower operation, and the EMP-DHRS (EMP6) was operated to maintain approximately $0.17\times10^{-3}$ $m^3/s$ (10 liter/min) for easy start of the transient test and to prevent sodium from freezing in the piping of the DHRS. Therefore, a certain amount of sodium at low temperatures was able to flow from the outlet of the D-DHX or the PHX during the tests.

It was difficult to ensure that flowrates were distributed equally for the inlets during the transient from the initial steady state at a high flowrate to the NC at a low flowrate. SV5 for the center assembly was fully opened and SV3 and SV4 for outer assemblies were opened to approximately 77%, to keep the flowrate equally distributed at a total of 2 % ($0.95\times10^{-3}$ $m^3/s$) of the NOC. Therefore, the flow distribution between the central and outer assemblies at the initial steady state was not balanced. The opening degree of SV1 was approximately 9 % to control the transient of flow coast-down from the initial state in the early transient.

### 5.3 Transient State

Figure 31 illustrates the prearranged time sequence of major components for the transient tests of Case-DRACS and Case-PRACS. Table 33 also lists the prearranged time sequence of component operations in Case-DRACS and Case-PRACS, as shown in Fig. 32. The operation sequence was almost the same in Case-DRACS and Case-PRACS except for the timing of SV2 valve closing in the SHTS as shown in Fig. 31(b).

In the PHTS shown in Fig. 31(a), to simulate the SCRAM of the SFR, the heater power was rapidly decreased to less than 10% of that at the initial state ($t$=0) as the total power. The power output was set lower than the decay heat curve for 30 s after the SCRAM to simulate the ratio of the power to the flowrate

and reproduce the core temperature changes of the SFR in the PLANDTL-DHX. After decreasing the heater power, it recovered to follow the transient curve of the decay heat power of the SFR. The flowrate balance of three inlet pipelines from the LP: Inlet-A for the center assembly, Inlet-B for three outer assemblies of A, B, and C, and Inlet-C for the other three assemblies of D, E, and F were regulated by the opening of the sodium valves SV3, SV4, and SV5 (see Figs. 2 and 31). The flowrate in the PHTS was reduced after the SCRAM to simulate the typical flow coast-down curve of the SFR. The opening degree of SV1 (see Figs. 2 and 31) gradually changed from approxmetry 9 % at 31 s to 100 % (full-open) at 110 s after the SCRAM to eliminate disturbance to the flow in the PHTS during DHRS operation. The flowrate decreased from the initial value at $5.7\times10^{-3}$ $m^3/s$ (12% of the NOC) to approximately $0.95\times10^{-3}$ $m^3/s$ (2% of the NOC) for 32 s, and the pump power of EMP1 was cut off at 60 s after the SCRAM. Thus, the flow in forced circulation through the PHTS was shifted to the NC under the thermal interactions of the SHTS via the IHX and DHRS after the SCRAM.

In the SHTS, as shown in Figs. 31(b-1) and (b-2) for Case-DRACS and Case-PRACS, the flowrate was decreased with reduced input power of EMP-2. The input power of EMP-2 was cut off at 48 s after the SCRAM. In Case-DRACS as shown in Fig. 31(b-1), the blower of AC-SHTS was closed at 40 s and the operation switched from FC to NC condition. The dumper of AC-SHTS and SV2 were closed at 2,400 s after the SCRAM and the flow in NC condition was stopped. In Case-PRACS as shown in Fig. 31(b-2), the blower of AC-SHTS was closed at 40 s. The dumper of AC-SHTS and SV2 were closed at 48 s and the flow was stopped.

In DHRS, as shown in Fig. 31(c), the dumper of AC-DHRS was opened at 60 s after the SCRAM, and the sodium flowrate driven by the EMF6 was increased from $0.17\times10^{-3}$ $m^3/s$ (10 liter/min) to $1.5\times10^{-3}$ $m^3/s$ (90 liter/min) from 60 to 110 s after the SCRAM. The blower of the AC-DHRS started at 80 s after the SCRAM to reach an air velocity of 7 m/s in 50 s.

**5.4 Transient Behaviors at Case-DRACS**

Figure 32 shows the transients of the measured data of (a-1) flowrate at the IHX inlet in the SHTS (F2), (b-1) total flowrate through the PHTS as F3+F4+F5, (c-1) flowrates at the inlets of assemblies of F3, F4, and F5, and (d-1) flowrate through DHRS as F6 for boundary conditions at Case-DRACS.

Figure 33 shows the transients of the measured data of (a-1) temperature at the inlet of the LP (T1), (b-1) temperature at the IHX inlet in the SHTS (T2), (c-1) temperatures at the inlets of assemblies (T3, T4, T5), and (d-1) temperature at the inlets of the DHX (T6) and PHX (T7) for the boundary conditions at Case-DRACS.

Figure 34 shows the transients of the measured data of (a-1) total heater power at the simulated core, (b-1) heater power at each segment in the simulated core, (c-1) heater powers at outer assemblies (A-C), and (d-1) at outer assemblies (D-F) in the simulated core for the boundary conditions at Case-DRACS.

Figure 35 (1) shows the transient of normalized pump head (PD1/PD1s) derived by the measured data of the EMP-PHTS (PD1) to the reference value (PD1s) at the steady state for the boundary condition at Case-DRACS. In the benchmark analysis, magnitude of PD1s can be evaluated as a parameter to balance the pressure losses in the primary loop at the steady state and the transition curve in the measured data can be used for the boundary condition.

### 5.5 Transient Behaviors at Case-PRACS

Figure 32 shows the transients of the measured data of (a-2) flowrate at the IHX inlet in the SHTS (F2), (b-2) total flowrate through the PHTS as F3+F4+F5, (c-2) flowrates at the inlets of assemblies of F3, F4, and F5, and (d-2) flowrate through DHRS as F6 for the boundary conditions at Case-PRACS.

Figure 33 shows the transient of the measured data of (a-2) temperature at the inlet of the LP (T1), (b-2) temperature at the IHX inlet in the SHTS (T2), (c-2) temperature at the inlets of assemblies (T3, T4, T5), and (d-2) temperature at the inlets of the DHX (T6) and PHX (T7) for boundary conditions at Case-PRACS.

Figure 34 shows the transients of the measured data of (a-2) total heater power at the simulated core, (b-2) heater power at each segment in the simulated core, (c-2) heater powers at outer assemblies (A-C), and (d-2) at outer assemblies (D-F) in the simulated core for the boundary conditions at Case-PRACS.

Figure 35 (2) shows the transient of normalized pump head (PD1/PD1s) derived by the measured data of the EMP-PHTS (PD1) to the reference value (PD1s) at the steady state for the boundary condition at Case-PRACS. In the benchmark analysis, magnitude of PD1s can be evaluated as a parameter to balance the pressure losses in the primary loop at the steady state and the transition curve in the measured data can be used for the boundary condition.

**Table 32 Steady-state conditions before SCRAM in each test case.**
**(Statistical mean values for 28 seconds before the SCRAM)**

| Case (ID. No.) | | | Case-DRACS*1 (24110) | Case-PRACS*1 (24115) |
|---|---|---|---|---|
| Power (MW) | Center assembly | Q1 | 144.9 (0.4) | 144.2 (0.4) |
| | Outer 3 assemblies of A-C | Q2 | 433.1 (0.7) | 434.8 (0.7) |
| | Outer 3 assemblies of D-F | Q3 | 431.1 (0.8) | 430.4 (0.9) |
| | Total power | Q1+Q2+Q3 | 1009.2 (1.0) | 1009.4 (1.3) |
| Flowrate ($10^{-3}$ $m^3/s$) | PHTS*2 | F1 | 5.712 (0.051) | 5.666 (0.049) |
| | SHTS | F2 | 5.641 (0.01) | 5.662 (0.009) |
| | RV inlet (Center) | F5 | 0.929 (0.004) | 0.923 (0.003) |
| | RV inlet (Outer A-C) | F3 | 2.330 (0.01) | 2.314 (0.01) |
| | RV inlet (Outer D-F) | F4 | 2.350 (0.012) | 2.318 (0.009) |
| | Total flowrate (as the PHTS flowrate) | F3+F4+F5 | 5.609 (0.019) | 5.554 (0.015) |
| | DHRS (DHX/PHX) | F6 | 0.170 (0.001) | 0.171 (0.002) |
| Inlet temperature (°C) | PHTS (LP inlet) | T1 | 301.6 (0.2) | 303.3 (0.2) |
| | SHTS (IHX inlet) | T2 | 265.8 (0.6) | 268.1 (2.6) |
| | RV inlet (Center) | T5 | 301.4 (0.3) | 302.8 (0.3) |
| | RV inlet (Outer A-C) | T3 | 301.8 (0.2) | 303.0 (0.2) |
| | RV inlet (Outer D-F) | T4 | 302.8 (0.2) | 304.2 (0.2) |
| | DHRS (DHX inlet) | T6 | 302.9 (0.2) | - |
| | DHRS (PHX inlet) | T7 | - | 288.6 (0.4) |

*1 The data presented below represent the average and standard deviation (in parenthesis) of 176 measurements obtained over 28 seconds with an interval of 0.16 seconds.

*2 Reference values that should not be used for the boundary condition.

**Table 33 Prearranged time sequence of component operations in Case-DRACS and Case-PRACS.**
**(see Fig. 31)**

| Time (s) | PHTS (Fig. 31 (a)) | SHTS | | DHRS (Fig. 31(c)) |
|---|---|---|---|---|
| | | Case-DRACS (Fig. 31(b-1)) | Case-PRACS (Fig. 31(b-2)) | |
| 0 (SCRAM) | - Heater power decreasing<br>- Flowrate at $5.7\times10^{-3}$ $m^3/s$ (12 % of the NOC(*)) | - AC-SHTS blower in operation and dumper 100 % open-Flowrate at $5.7\times10^{-3}$ $m^3/s$ (400 liter/min for 12 % of the NOC) | | - AC-DHRS blower off<br>- AC-DHRS dumper close<br>- Flowrate at $0.17\times10^{-3}$ $m^3/s$ (10 liter/min) |
| 15 | - Flowrate decreasing to $1.0\times10^{-3}$ $m^3/s$ (2% of the NOC) | - EMP2 power decreasing<br>- AC-SHTS blower decreasing | | |
| 31 | - SV1 valve opening from 9 % to 100 % | | | |
| 32 | - Flowrate at $1.0\times10^{-3}$ $m^3/s$ (2 % of the NOC) | | | |
| 40 | | - AC-SHTS blower off | | |
| 48 | | - EMP2 power off | | |
| | | | - AC-SHTS dumper close<br>- SV2 close | |
| 60 | - EMP1 power off | | | - Flowrate increasing<br>- AC-DHRS dumper open start |
| 80 | | | | - AC-DHRS blower increasing |
| 110 | - SV1 valve at 100 % open | | | - Flowrate at $1.5\times10^{-3}$ $m^3/s$ (90 liter/min) |
| 130 | | | | - AC-DHRS blower at 7 m/s |
| 2400 | | - AC-SHTS dumper close<br>- SV2 close | | |

(*) NOC: Normal operating condition of a large-scale SFR

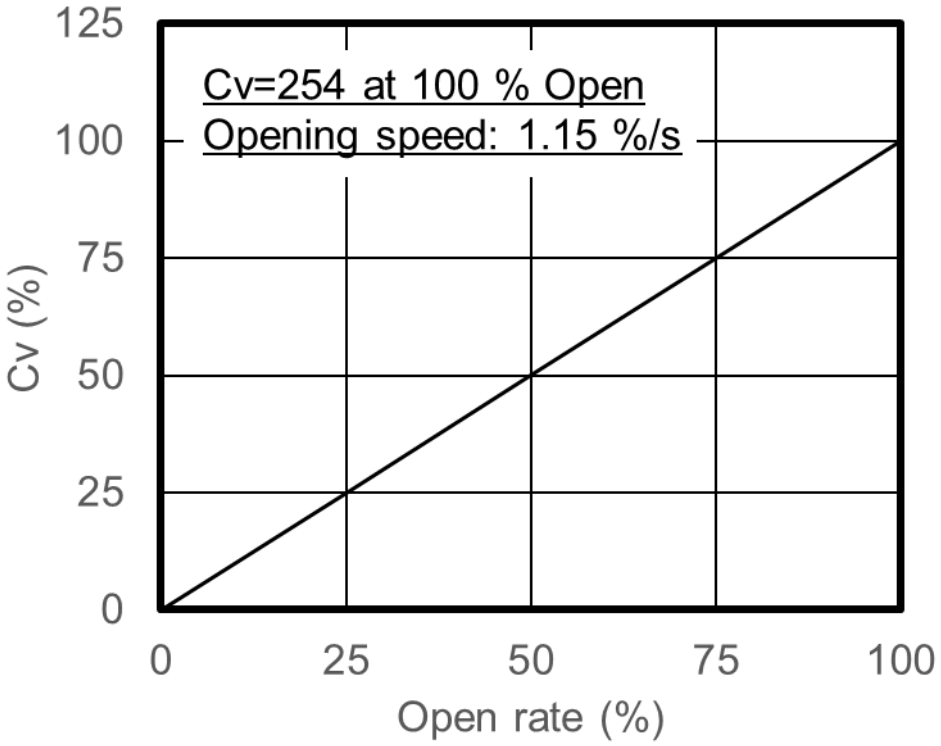


**Figure 30 Performance specification on valve flow coefficient (Cv) of SV1 (SV101M) .**

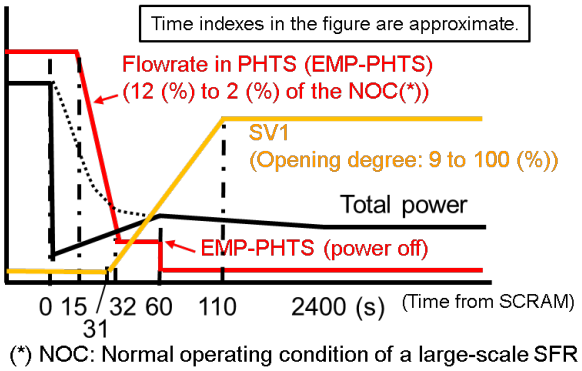


**(a) Major components in PHTS**

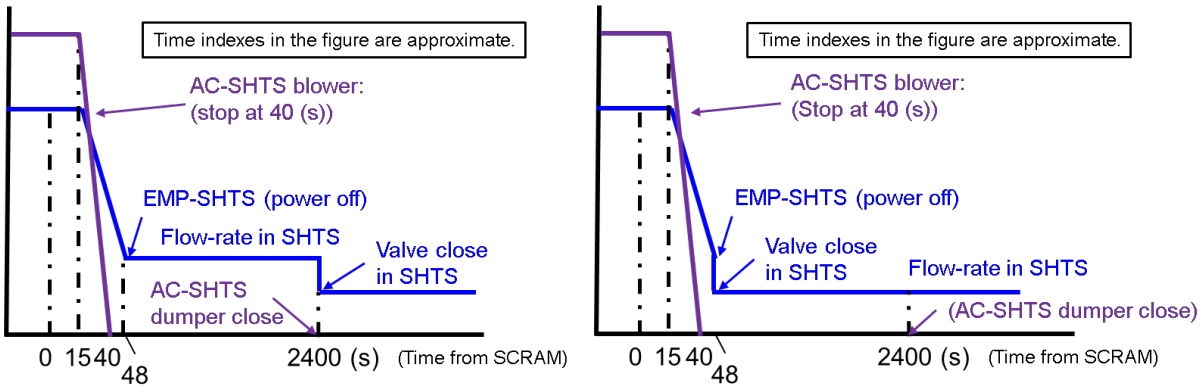


**(b-1) Case-DRACS** **(b-2) Case-PRACS**

**(b) Major components in SHTS**

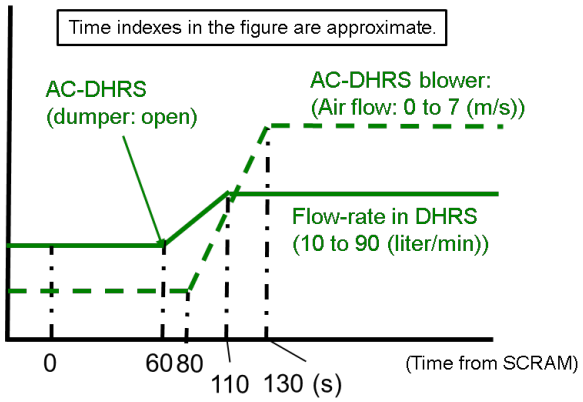


**(c) Major components in DHRS**

**Figure 31 Prearranged time sequences of major components for test setting. (see Table 33)**

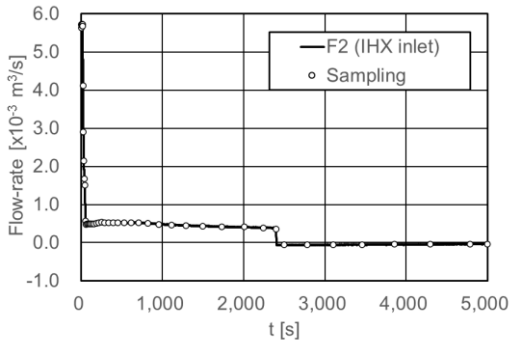


(a-1)

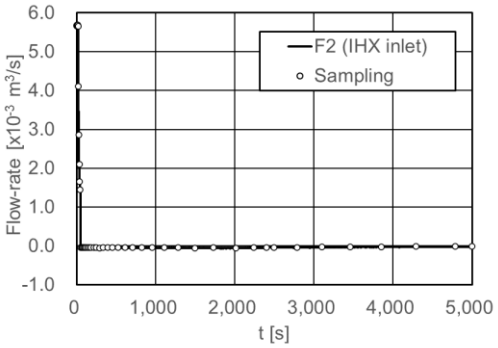


(a-2)

**(a) Flowrate at IHX inlet in SHTS (F2)**

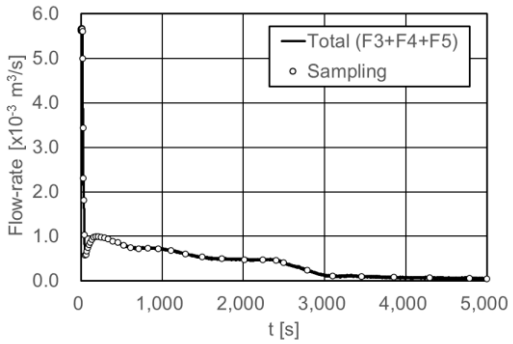


(b-1)

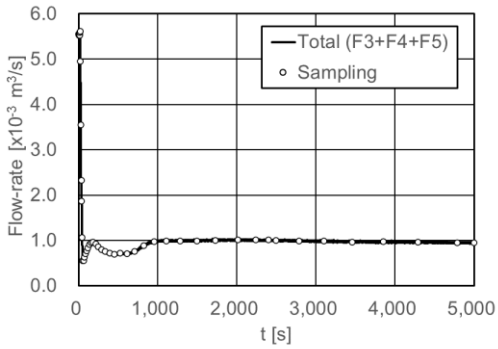


(b-2)

**(b) Total flowrate through PHTS (F3+F4+F5)**

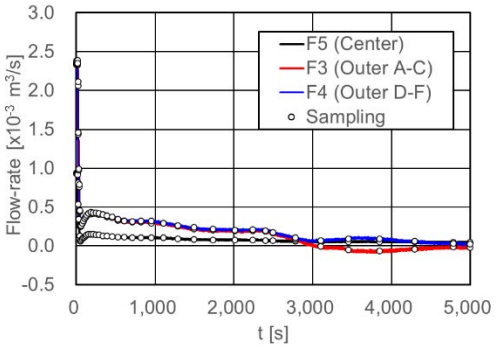


(c-1)

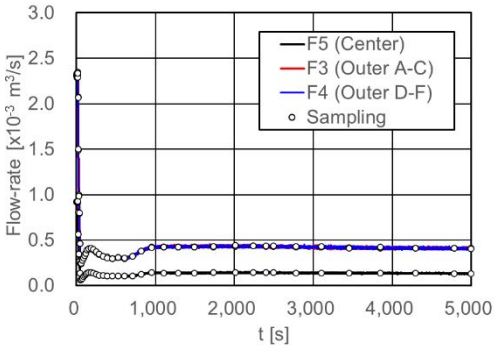


(c-2)

**(c) Flowrate at the inlets of assemblies (F3, F4, F5)**

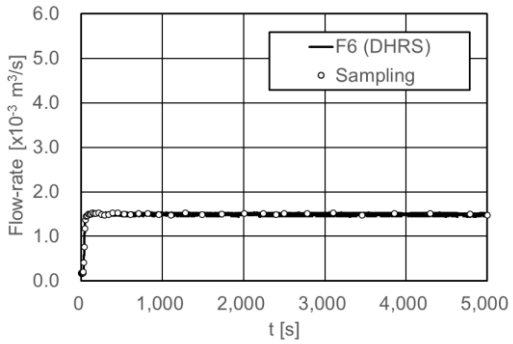


(d-1)

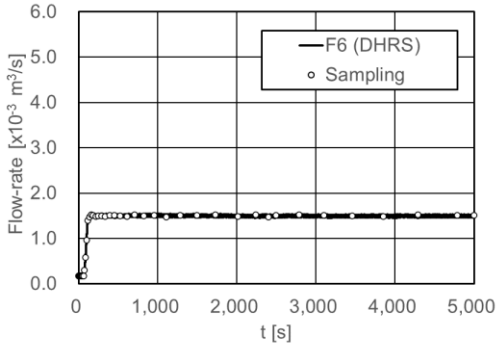


(d-2)

**(d) Flowrate through DHRS (F6)**

**Figure 32 Transient of measured flowrate for (1) Case-DRACS and (2) Case-PRACS.**

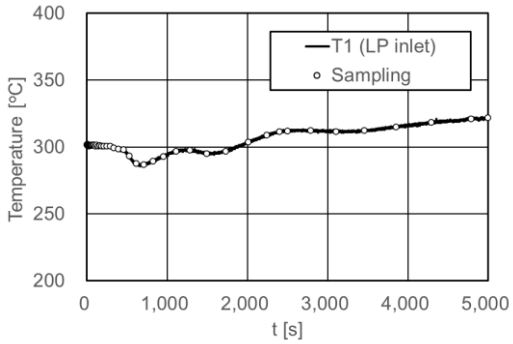


(a-1)

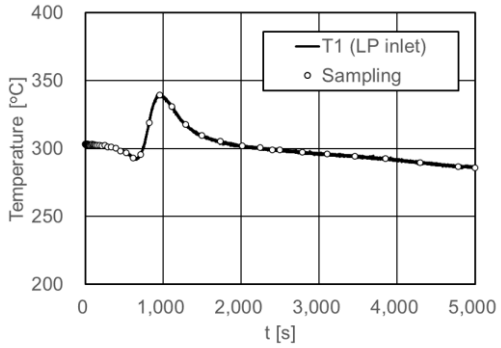


(a-2)

**(a) Temperature at LP inlet(T1)**

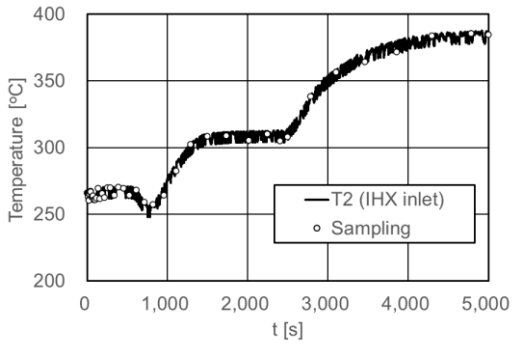


(b-1)

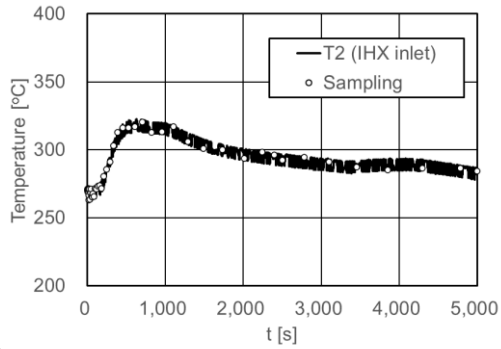


(b-2)

**(b) Temperature at IHX inlet in SHTS (T2)**

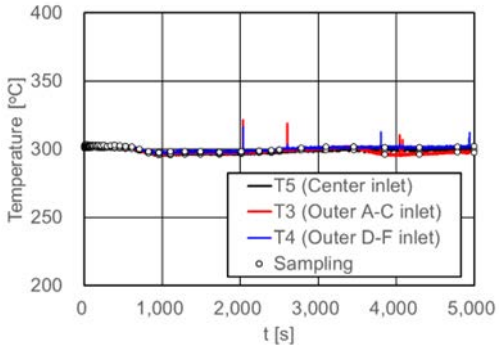


(c-1)

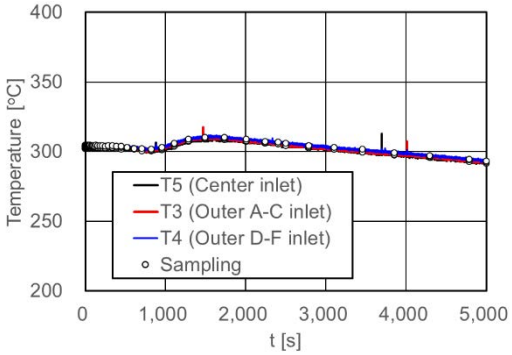


(c-2)

**(c) Temperature at the inlets of assemblies (T3, T4, T5)**

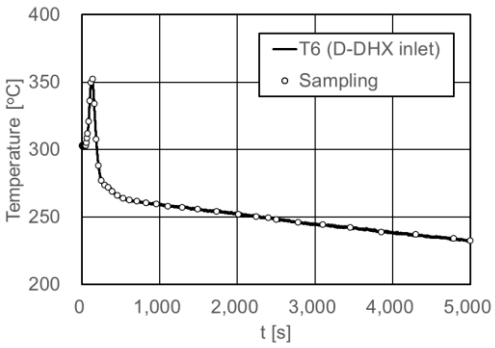


(d-1)

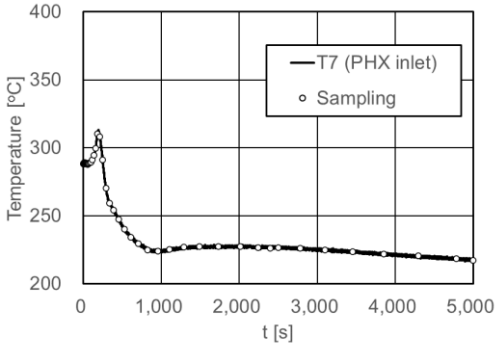


(d-2)

**(d) Temperature at the inlets of D-DHX (T6) and PHX (T7)**

**Figure 33 Transients of measured temperatures for (1) Case-DRACS and (2) Case-PRACS.**

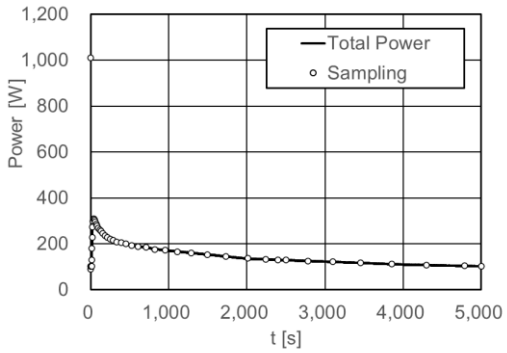


(a-1)

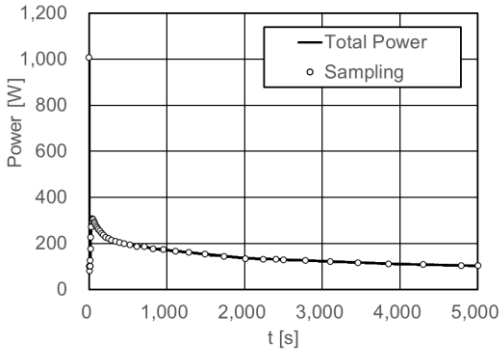


(a-2)

**(a) Total heater power at the simulated core**

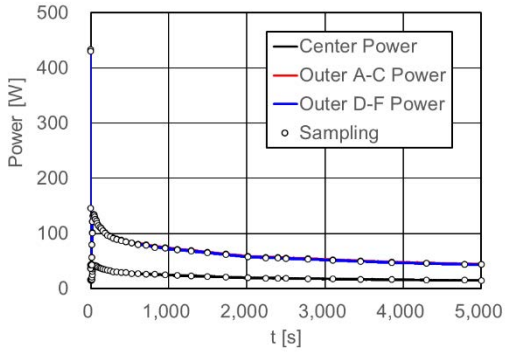


(b-1)

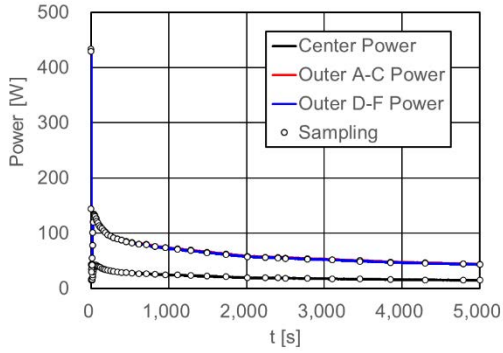


(b-2)

**(b) Heater power at each segment in the simulated core**

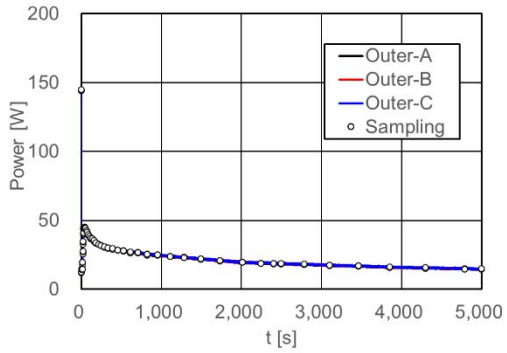


(c-1)

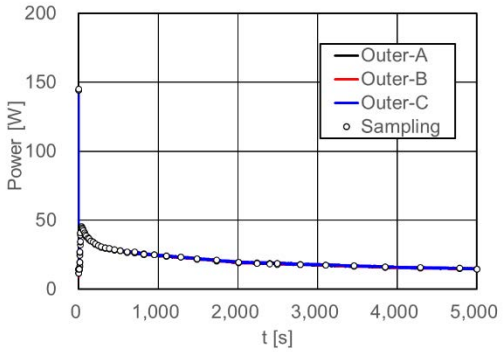


(c-2)

**(c) Heater powers at outer assemblies (A-C) in the simulated core**

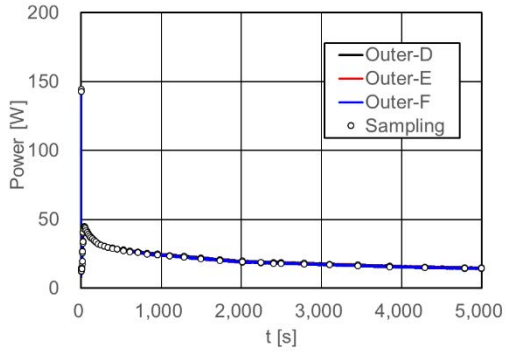


(d-1)

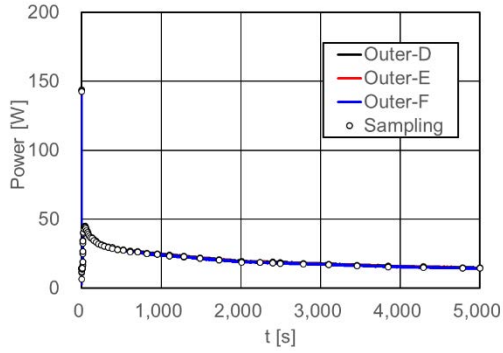


(d-2)

**(d) Heater powers at outer assemblies (D-F) in the simulated core**

**Figure 34 Transients of measured heater power for (1) Case-DRACS and (2) Case-PRACS.**

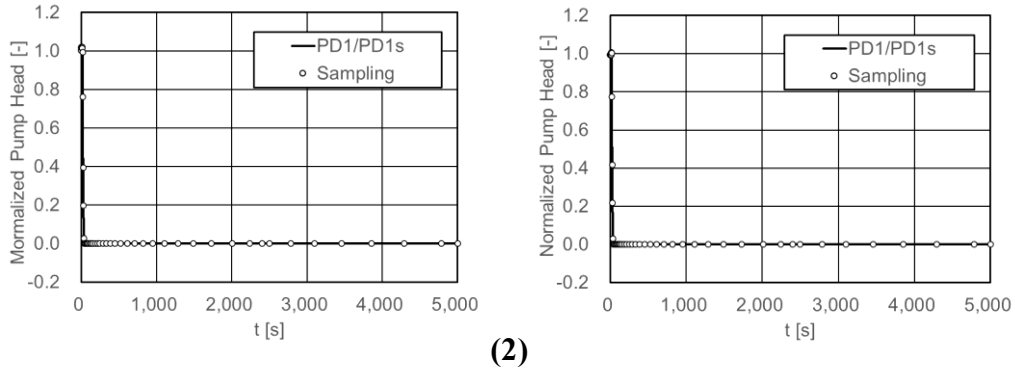


**(1)** **(2)**

**Figure 35 Transient of normalized pump head for (1) Case-DRACS and (2) Case-PRACS.**

## 6. Summary

The data of two transient tests using the DRACS and PRACS conducted at the PLANDTL-DHX were provided with the dimensions of the RV and the PHTS including the heat exchangers for DHRS, as well as the boundary conditions of the measured flowrate and temperature changes at the inlets of the intermediate heat exchanger (IHX) and DHRS on the secondary side, to implement the benchmark analysis for the validation of the modeling and simulation.

In Case-DRACS, the cold sodium coming from the D-DHX occupies the lower region of the UP-RV and thermal stratification appears in it. The cold sodium from the D-DHX enters the core region. The IWF can remove the heat generated in the assemblies through their wrapper tubes. The RHT among assemblies through the sodium in the IWG can flatten the horizontal temperature distribution in the core and the flowrates through the assemblies are redistributed according to the temperature distribution in the core. In Case-PRACS, the flowrate of the PHTS regulating the maximum temperature in the core is affected by the operating conditions of the SHTS and DHRS. Complex thermal-hydraulic behavior such as CPI is not significant in the RV.

To develop an appropriate numerical analysis model for the prediction of transient thermal-hydraulics in the core, the PHTS, and the DHRS, the dimensions of the components, including the UP-RV, simulated core, LP in the RV, IHX, D-DHX in the DRACS, and PHX in the PRACS, were described. Moreover, other components in the PHTS, SHTS, and DHRS are also described in Chap. 2 for easy understanding of the plant dynamics. In Sec. 3, a coupled analysis model using plant dynamics analysis code for the elements in the heat transport system and multi-dimensional CFD code for the RV was selected as a reference model in the benchmark analyses, while it was allowable to construct another appropriate model by the participant. Section 4 describes the locations where the benchmark data, including the flowrates in the PHTS and temperatures in the UP-RV, simulated core, PHTS, SHTS, and DHRS, were measured for comparison with the numerical results. In Sec. 5, boundary conditions based on the measured data for benchmark analyses are provided for the initial steady state and the transient state in Case-DRACS and Case-PRACS.

**References**

[1] S. Kubo, Y. Chikazawa, H. Ohshima, M. Uchita, T. Miyagawa, M. Eto, T. Suzuno, I. Matoba, J. Endo, O. Watanabe, and K. Higurashi, A conceptual design study of pool-type sodium-cooled fast reactor with enhanced anti-seismic capability, Bulletin of the JSME, Mechanical Engineering Journal, Vol.7, No.3, 2020, 19-00489. [DOI: 10.1299/mej.19-00489]

[2] H. Kamide, K. Hayashi, T. Isozaki, and M. Nishimura, Investigation of core thermohydraulics in fast reactors – Interwrapper flow during natural circulation, Nuclear Technology, Vol.133, pp.77-91 (2001).

[3] H. Kamide, N. Kimura, K. Hayashi, and M. Nishimura, Experimental Study on Inter-Wrapper Flow during Natural Circulation in Fast Reactors - Influence on Natural Circulation Flow and Core Temperatures, Proceedings of the 6th International Conference on Nuclear Engineering (ICONE6), San Diego, California, May 10-14, 1998, ICONE-6197.